High-grade Palaeoproterozoic reworking in the southeastern Gawler Craton, South Australia.

Rian Dutch[a *], Martin Hand[a] & Peter Kinny[b]

[a] Continental Evolution Research Group, School of Earth and Environmental Sciences, University of Adelaide, S.A. 5005, Australia.

[b] School of Applied Geology, Curtin University of Technology, W.A. 6102, Australia.

*Corresponding Author; DP313, School of Earth and Environmental Sciences, University of Adelaide, South Australia, 5005.
Tel.: +61 8 8303 4971; fax: +61 8 8303 4347
E-mail address: rian.dutch@adelaide.edu.au

Document Processed using Microsoft Office Word 2003

ABSTRACT

SHRIMP U-Pb geochronology and monazite EPMA chemical dating from the southeast Gawler Craton has constrained the timing of high grade reworking of the early Palaeoproterozoic (c. 2450 Ma) Sleaford Complex during the Palaeoproterozoic Kimban Orogeny. SHRIMP monazite geochronology from mylonitic and migmatitic high-strain zones that deform the c. 2450 Ma peraluminous granites indicates that they formed at 1721 ± 3 and 1725 ± 2 Ma. These are within error of EPMA monazite chemical ages of the same high-strain zones which range between 1691 Ma and 1736 Ma. SHRIMP dating of titanite from peak metamorphic (10 kbar at 730°C) mafic assemblages give ages of 1712 ± 8 and 1708 ± 12 Ma. The post-peak evolution is constrained by partial to complete replacement of garnet – clinopyroxene bearing mafic assemblages by hornblende – plagioclase symplectites, which record conditions of c. 6 kbar at 700°C, implying a steeply decompressional exhumation path. The timing of Palaeoproterozoic reworking corresponds to widespread deformation along the eastern margin of the Gawler Craton and the development of the Kalinjala Shear Zone.

Keywords: Gawler Craton, reworking, SHRIMP, Kimban Orogen, P-T evolution, EPMA monazite

1. Introduction

The Gawler Craton, in southern Australia (fig. 1), has a protracted tectonic, metamorphic and magmatic history spanning the late Archaean to the Mesoproterozoic (e.g. Daly et al., 1998; Fanning et al., 2007). Despite being a region of exceptional economic potential the evolutionary framework for the Gawler Craton is still poorly constrained. Many of the ambiguities surrounding the evolution of the Gawler Craton revolve around the timing, spatial distribution and thermobarometric conditions of the tectonic events, which have affected the craton (Daly et al., 1998; Fanning et al., 1988; Fanning et al., 2007; Ferris et al., 2002).

Two of the most widespread tectonic intervals represented on the Gawler Craton are the Late Archaean to earliest Proterozoic Sleafordian Orogeny (c. 2440-2420 Ma, Daly & Fanning, 1993; Fanning et al., 1988; Fanning et al., 2007) and the Palaeoproterozoic Kimban Orogeny (c. 1730-1690 Ma, Fanning et al., 2007). Previous workers (e.g. Daly & Fanning, 1993; Fanning et al., 1988) have suggested that the Late Archaean core of the Gawler Craton has been ubiquitously affected by the Sleafordian Orogeny, which was then overprinted by the younger Kimban Orogeny. Despite the importance of the Kimban Orogeny in the structural and metamorphic evolution of the southern Gawler Craton, and its importance in the recently proposed reconstructions of the Australian Proterozoic (Betts & Giles, 2006; e.g. Giles et al., 2004; Wade et al., 2006), there is surprisingly little published geochronological data directly constraining the timing of fabric development and metamorphism (e.g.Jagodzinski et al., 2006; Reid et al., 2007; Swain et al., 2005a).

Previous descriptions of the Kimban Orogeny have focused on the eastern Eyre Peninsula, where Kimban deformation was thought to be controlled by high-grade

deformation along the Kalinjala Shear Zone and its hinterland (e.g. Parker, 1993; Vassallo & Wilson, 2002). However, little information was known about the extent of Kimban aged deformation to the west of this region.

In this study we present the timing of high grade reworking from the western Eyre Peninsula (fig. 2). A combination of structural mapping and thermobarometric analysis has been used to determine the geological evolution of the Coffin Bay Peninsula and the pressure-temperature conditions of the metamorphism recorded in deformed metabasic dykes. This has been coupled with EPMA monazite chemical dating from shear zones and SHRIMP U-Pb dating of metamorphic monazite and metamorphic titanite from the mafic assemblages.

The results show that high-grade reworking on the western Eyre Peninsula, reflecting lower crustal conditions, occurred between 1724 – 1708 Ma during the Kimban Orogeny. These results imply that the metamorphic architecture of the Kimban Orogen in the south-eastern Gawler Craton is defined by panels of dramatically contrasting metamorphic grade, reflecting large local gradients in the degree of exhumation.

2. Regional Geology

The Gawler Craton, southern Australia (fig. 1) consists of a late Archaean to Palaeoproterozoic core (Daly & Fanning, 1993; Daly et al., 1998; Fanning et al., 1988; Fanning et al., 2007; Swain et al., 2005b), surrounded by Palaeoproterozoic to Mesoproterozoic metasediments and igneous suites (Fanning et al., 1988; Parker, 1993; Daly et al., 1998; Ferris et al., 2002; Fanning et al., 2007). The craton preserves a protracted history of deformation, metamorphism, sedimentation and magmatism

spanning approximately 1100 Myrs from c. 2500 Ma to c. 1450 Ma (Daly et al., 1998; Fanning et al., 2007; Ferris et al., 2002).

On Eyre Peninsula (fig. 2), the late Archaean to Palaeoproterozoic Sleaford Complex (Thomson, 1980) is unconformably overlain by the Palaeoproterozoic Hutchison group metasediments and Donnington Suite granitoids to the east (Daly & Fanning, 1993; Parker 1993; Fanning et al., 2007; Daly et al., 1998, Schwarz et al., 2002). The Sleaford Complex (Fig. 2) consists of the late Archaean high grade Carnot Gneisses, the amphibolite facies Wangary Gneiss, the greenschist facies Hall Bay Volcanics and the supracrustal intrusives of the Dutton Suite (Daly & Fanning, 1993; Fanning et al., 2007).

The Dutton Suite forms a major high crustal-level batholith, which forms a volumetrically significant portion of the western Eyre Peninsula and outlying islands off the Coffin Bay Peninsula (fig, 2). The Dutton Suite consists primarily of the early-formed Coulta Granodorite (2519 ± 8 Ma; Fanning et al., 2007), the Kiana Granite (2462 ± 15 and 2466 ± 11 Ma; Fanning et al., 2007), the Whidbey Granite (2445 ± 4 Ma; Jagodzinski et al., 2006) and other minor undifferentiated granitoid intrusions. The rocks of the Coffin Bay region (fig. 2) are dominated by granitic lithologies of the Dutton Suite that intruded during the c. 2480-2420 Ma Sleafordian Orogeny (Fanning et al., 2007; Swain et al., 2005b). The granites are dominated by peraluminous compositions with garnet and garnet-cordierite bearing tabular K-feldspar varieties (fig. 3a), with minor outcrops of a cordierite leucogranite.

The metamorphic conditions attained during the Sleafordian Orogeny are recorded by granulite-facies mineral assemblages in metasedimentary lithologies in the Cape Carnot region approximately 50 km east of the Coffin Bay Peninsula region (fig. 2, Daly et al., 1998; Fanning et al., 1981), however, there is no evidence of

metamorphosed sedimentary units on the Coffin Bay Peninsula. Aside from discrete zones of high-grade reworking (see below), the granites in the Coffin Bay region are largely undeformed, suggesting they mostly post-date Sleafordian-aged deformation. The undeformed granites often contain well-developed magmatic flow fabrics defined by aligned tabular feldspar phenocrysts up to 5 cm in length, (fig. 3a) trending north to northeast.

The granites of the Coffin Bay Peninsula have been intruded by a series of mafic dykes, which generally trend north-east (fig. 3b). The dykes are between 3 and 50 m's wide and have been variably deformed and recrystallised.

To the immediate east of the Coffin Bay Peninsula extending north to Drummond Point lie the Archaean aged chloratoid – andalusite bearing Hall Bay Volcanics (Fanning et al., 2007; Swain et al., 2005b). Overlying this unit is the c. 1760 Ma greenschist facies phyllitic schists of the Price Metasediments (Fig. 2, Oliver & Fanning, 1997). To the east of these units lie the late Archaean Wangary Gneisses (Fanning et al., 2007). Outcrops of the Wangary Gneiss at the Frenchmans and Coles Point (fig. 2) consist of a muscovite – biotite – andalusite stable schist (fig. 3c), indicating these rocks have never experienced pressures above the stability field of andalusite (c. 4 kbar).

2.1. Tectonothermal events of the southern Eyre Peninsula

Parts of the southern Eyre Peninsula record the affects of at least two deformation/metamorphic events. The Sleafordian Orogeny (c. 2440-2420 Ma; Fanning et al. 1988; Daly and Fanning, 1993; Daly et al., 1998) is characterised by high temperature-low pressure (HTLP) greenschist to granulite facies metamorphism

126 (Daly & Fanning, 1993; Fanning et al., 1981; Schwarz, 2003a), which affected the
127 late Archaean component of the Eyre Peninsula (fig. 2). Little is known about the
128 tectonic setting or structural evolution of this event as it has been thoroughly
129 overprinted by subsequent events.
130 The Kimban Orogeny (c. 1730-1690 Ma) dominates the tectonic architecture of
131 the southern Eyre Peninsula, overprinting all earlier fabric systems (Parker, 1993;
132 Swain et al., 2005a; Vassallo & Wilson, 2002; Webb et al., 1982; Webb et al., 1986).
133 The most obvious expression of the Kimban Orogeny is the development of the
134 Kalinjala Shear Zone (fig. 2). This forms a subvertical high-strain zone up to 6 km
135 wide and c. 400 km long, along the eastern edge of the peninsula (Parker, 1980);
136 Parker et al., 1993; Vassalo and Wilson, 2002). The Kalinjala Shear Zone separates
137 the Sleafordian aged rocks and younger cover sequences of the Hutchison Group from
138 the 1850 Ma Donnington Granitoid Suite, which comprises the bulk of the south-
139 eastern Gawler Craton (fig. 2).
140 Intense Kimban aged deformation and metamorphism is localised into a domain
141 ~50 km wide around the Kalinjala Shear Zone (fig. 2), with 10 kbar granulite-facies
142 rocks within the core of the shear zone and lower P (6 kbar) granulites on the flanks of
143 the shear zone (Hand et al., 1995; Tong et al., 2004). The metamorphic grade
144 decreases to low-P amphibolite facies to the north of the peninsula (Parker et al.,
145 1993), suggesting the structure has an overall obliquity in its along strike exposure.
146 In the Hutchison Group (fig. 2), north-directed layer parallel transport evolved
147 into non-cylindrical fold systems that parallel the overall transport vector along the
148 orogen (Vassalo and Wilson, 2002). In the Donington Suite, discreet mylonite zones
149 more commonly express the deformation (Parker et al., 1993; Vassalo and Wilson,

2002). Macro-scale drag into the Kalinjala Shear Zone suggests it developed mainly in a dextral transpressive regime (Vassallo and Wilson, 2002).

To the west of the Kalinjala Shear Zone, metamorphic intensity decreases dramatically to the extent that late Archaean volcanoclastic rocks of the Hall Bay Volcanics and the Wangary Gneiss along with the c. 1760 Ma Price metasediments in the central Eyre Peninsula contain greenschist to lower amphibolite grade assemblages (Oliver & Fanning, 1997; Swain et al., 2005b). Geochronological studies from the western Eyre Peninsula using K-Ar, Ar-Ar and Rb-Sr methods on micas indicate that the region reached c. 500 °C at c. 1673 Ma (Nebel et al., 2007) and cooled through c. 400 °C by 1650 Ma (Foster & Ehlers, 1998; Webb et al., 1982) and c. 300 °C by 1620 Ma (Foster & Ehlers, 1998; Webb et al., 1982).

3. Structural reworking of the Coffin Bay Peninsula

The coastline of the Coffin Bay Peninsula (fig. 4) preserves a limited window into the late Archaean granitic basement of the southwestern Eyre Peninsula. The earliest fabric developed is a weak magmatic fabric ($S_{granite}$) defined by aligned tabular feldspar grains within the peraluminous granite (fig. 3a). This fabric generally trends NW to NE and predates all other fabric development having occurred during the emplacement of the granite body (fig. 4).

The main structural elements, besides the pre-existing weakly developed magmatic fabric, are a number of strongly developed sub-mylonitic to mylonitic and migmatitic shear fabrics (both S_1 and S_2), ranging in width from 30 cm to approximately 300 m, which have reworked the Sleafordian-aged granites and mafic dykes (fig. 4) and obliterated the pre-existing weak magmatic fabric in the granites.

These shear zones predominantly trend N to NE and dip to the west (S_1; fig. 4). A small subset of shear zones trend E-W (S_2; fig. 4). Overprinting relationships indicate that the E-W shear zones (S_2) post date the N to NE orientated (S_1) shear system. However, there is no discernable petrological or kinematic difference between the S_1 and S_2 structures, and they are therefore interpreted to have formed during the same deformation event (S_2 structures, like S_1, consist of both mylonitic and migmatitic shear zones). Well developed mineral stretching lineations (L_1, L_2) occur on both the S_1 and S_2 surfaces (L_1 and L_2 are parallel). South of Mullalong Beach (fig. 4) L_1 and L_2 plunge moderately to the SW, while in the Point Sir Isaac region L_1 plunges shallowly to the NE (fig. 4).

Kinematic indicators within both S_1 and S_2 shear zones indicate both dextral west block up, and sinistral west block down movement directions. On the west coast at Mullalong Beach and Pt Sir Isaac south (fig. 4), S-C fabrics and porphyroclast systems indicate predominantly dextral, west block to the NE movement. At all other localities S-C fabrics, porphyroclast systems and asymmetric flow perturbation folds (fig. 3d) indicate an apparently sinistral extensional (west block down) kinematic setting (fig. 4). This apparent conflict between dextral and sinistral shear zone movement on either side of the peninsula is discussed in more detail below.

The bulk of the shear zones on the Coffin Bay Peninsula are developed in felsic lithologies, now represented by either fine-grained discrete sub-mylonites to mylonites (fig. 3e) or, in the case of the larger shear zones, stromatic migmatites. There is no observed difference in orientation, structural setting or timing between the mylonitic and the migmatitic shear zones and they are therefore interpreted to be structurally equivalent (both S_1 and S_2 structures, with S_2 slightly post-dating S_1 development).

Sub-mylonitic to mylonitic shear zones within felsic lithologies contain a strong foliation defined predominantly by a bimodal quartz – feldspar grain size distribution with mostly fine grained dynamically recrystallised grains together with large relic grains which show undulose extinction. Shear fabrics developed in the deformed mafic dykes vary in intensity, from a well-defined foliation defined by an alignment of hornblende, through to a mylonitic fabric defined by highly deformed plagioclase ± quartz ribbons (fig. 3f).

Within the felsic migmatitic shear zones, leucosome volume ranges between c. 2-10%. Leucosomes range in thickness between 1 and 10cm and both parallel and crosscut the shear fabric, in places forming syn- to post-kinematic vein networks (fig. 3g). In migmatitic mafic dykes, garnet ± clinopyroxene-bearing felsic segregations have been deformed into foliation-defining structural elements (fig. 3f), but also locally occur as undeformed segregations that crosscut the hornblende foliation (fig. 3h).

Due to the limited outcrop and the paucity between exposures, it is not possible to map the S_1 and S_2 shear zones out in their entirety. It is therefore difficult to place the development of the shear zones into an overall model, especially considering the apparently conflicting kinematics. One possibility is that the shear zone fabrics define the limbs of a regional scale, doubly plunging (NE and SW) fold system (e.g. Goscombe & Trouw, 1999). The orientations of the shear fabrics when plotted on a stereonet define a girdle which suggests a NE trending fold axis (fig. 4). The asymmetry of data along this girdle, with a predominance of westerly dipping foliations, suggests this fold system is east-vergent (fig. 4). Unfolding this structure resolves the apparent opposing kinematics seen on opposite sides of the peninsula (fig. 4a & b), and indicates that the shear zone system developed in a regionally

225 dextral, transpressional setting, analogous to the development of the Kalinjala Shear
226 Zone on the east coast (fig. 2).
227
228 **4. Petrography of the Shear Zones**
229
230 *4.1. Petrography of the felsic shear zones*
231
232 Mylonitic felsic shear zones are dominated by an assemblage of qtz – ksp – pl
233 ± minor bi (fig. 3d; abbreviations after Kretz, 1983). In the migmatitic shear zones,
234 leucosomes occasionally contain garnet, however the bulk of the leucosomal
235 segregations in deformed granites lack an Fe-Mg peritectic phase. The fabric in the
236 intervening (non leucosomal) shear zone volume is predominantly defined by an
237 assemblage identical to that of the mylonitic shear zones (qtz – ksp – pl ± bi) although
238 in places it also contains sillimanite as a minor component. Garnet-bearing shear
239 fabric assemblages are comparatively uncommon with garnet only being found in
240 regions of lower strain where it forms sub-hedral crystals surrounded by a fsp – qtz –
241 sill ± bi assemblage (fig. 5a). Cordierite appears to be entirely absent from all shear
242 zone assemblages despite being present in the undeformed granitic wall rocks.
243
244 *4.2. Petrography of the metabasites*
245
246 Metabasic rocks in the Coffin Bay region contain a peak assemblage of grt – cpx –
247 hbd $_{(\text{high Ti})}$ – pl – qtz, with accessory ilmenite and titanite (fig. 5b). Igneous textures
248 are not preserved. The peak assemblage of grt – cpx probably formed via the
249 dehydration reaction:

hbd $_{(low\ Ti)}$ + pl + qtz + ilm = grt + cpx + hbd $_{(high\ Ti)}$ + tit + melt

(e.g. Pattison, 2003; Wolf & Wyllie, 1994). This reaction is texturally consistent with the observation that the majority of the hornblende assemblage is high in Ti (Table 1). Titanite contains inclusions of ilmenite and occurs as inclusions in high Ti hornblende but not as inclusions in the other peak porphyroblastic phases. The majority of the grt – cpx segregations have then undergone the near isothermal fluid induced break down reaction (e.g. Harley, 1989; Pattison, 2003):

grt + cpx + L = pl + hbd $_{(low\ Ti)}$ + qtz

This is a common metamorphic reaction in terrains which have undergone significant decompression (e.g. Harley, 1989; Mawby et al., 1999; Zhao et al., 2000). This reaction has occurred to various extents in different samples, with some samples showing complete replacement of peak grt – cpx, which are now represented by fine-grained intergrowths of hbd $_{(low\ Ti)}$ – pl – qtz (fig. 5c).

Deformation of the metabasites is interpreted to have occurred during metamorphism because garnet bearing partial melts cross-cut the shear foliation and the post-peak mineral assemblage (hbd – pl – qtz intergrowths) are wrapped by the shear foliation.

5. Thermobarometric constraints on metamorphism.

The thermobarometric conditions for each of the selected metabasite assemblages were calculated via the average-P and average-T approach (Powell & Holland 1994) using the computer program THERMOCALC v3.25 (Powell & Holland, 1988) and the 2003 update of the Holland & Powell (1998) internally consistent dataset (v5.5).

Activity-composition relationships for minerals used in calculations were calculated using the software AX2000 (Holland & Powell 1998).

Mineral compositions of assemblages within metabasites and felsic shear zones were obtained using a Cameca SX51 Electron Microprobe, located at the University of Adelaide. Quantitative analyses were run at an accelerating voltage of 15 kV and a beam current of 20 nA. Representative mineral analyses are given in Table 1. Detailed mineral chemistry for all analysed samples can be found online as a supplementary publication. Calculations were preformed using a number of different H_2O activities to gage the effect this would have on the final P and T result. No significant difference was found and as the mineral assemblage is hydrous an H_2O activity of 1 was used.

In order to explore the compositional character of garnets from the metabasites, individual garnets were compositionally profiled for the elements Fe, Mg, Mn and Ca (fig. 6). Quantitative garnet cation profiles from garnet rim to rim were run at an accelerating voltage of 15 kV and a beam current of 20 nA.

Garnet cation profiles are typically flat, consistent with the values obtained through spot analysis (e.g. fig. 6, sample SB 4). Some garnet grains which had undergone the least amount of retrograde resorption showed a slightly bell shaped curve for Mn with higher concentrations in the core and lower towards the rim (e.g. fig. 6, sample SB 31). This is typical of prograde growth zoning (e.g. Spear, 1993) and is probably a relict of the up temperature path. The higher X_{Mn} value appears to be accommodated by a slight decrease in X_{Fe}.

All P-T results for each sample are presented in Table 2. All analysed samples contained the assemblage hbd – pl – cpx – grt – qtz – ilm – tit. All pooled pressures and temperatures are weighted averages with quoted errors at 2σ. Average peak pressures obtained from the core compositions of minerals from metabasite

assemblages range from 9.5 kbar up to 10.6 kbar with uncertainties up to 1 kbar. Average peak temperatures range from 713°C to 763°C with uncertainties up to 57°C. Post peak metamorphic conditions obtained from two samples with almost completely reacted out garnet – clinopyroxene produced an average pressure of 7.1 ± 1.4 kbar at an average temperature of 785 ± 100 °C, consistent with the decompression textures observed in the rock.

The calculated P-T conditions from the felsic shear zones was done via the average-PT approach of THERMOCALC and was consistent with pressures and temperatures obtained via the average-P and average-T methods. Conditions of 701 ± 53 °C at 5.2 ± 2 kbar were obtained from mineral compositions of grt – bi – pl – ksp – ilm – qtz – sill assemblages. These conditions are consistent with the P-T values obtained from the post-peak mafic assemblages.

6. Age constraints on deformation and metamorphism

A combination of EPMA monazite and SHRIMP monazite and titanite geochronology was undertaken in order to constrain the timing of metamorphism recorded in the metabasites and felsic shear zones. Monazite EPMA chemical dating was undertaken as reconnaissance geochronology on a number of migmatitic and mylonitic shear zones from around the peninsula (fig. 4). However, as there can be large errors associated with EPMA geochronology (up to ±25 Ma), SHRIMP dating was also used to better constrain the ages. Monazite was selected as it was ubiquitous within the felsic samples and was believed to be more suited than zircon to record the age of reworking and less prone to inheritance. Titanite was selected from the

323 metabasites as it was the only accessory mineral amenable to U-Pb dating techniques
324 within the peak assemblage.
325
326 *6.1. EPMA Monazite Chemical Dating Analytical Techniques*
327
328 EPMA monazite chemical dating (e.g. Montel et al., 1996; Williams &
329 Jercinovic, 2002), uses an electron microprobe to measure the total amounts of U, Th
330 and Pb in monazite. Monazite is typically very rich in the radioactive elements U and
331 Th, and typically contains negligible common Pb compared with the radiogenically
332 produced component (e.g. Parrish, 1990), therefore it can be reasonably assumed that
333 essentially all measured Pb in monazite is the result of the radiogenic breakdown of
334 Th and U.
335 Analyses of monazite were conducted using a Cameca SX51 Electron Microprobe, at
336 Adelaide Microscopy in the University of Adelaide. The analyses were run at an
337 accelerating voltage of 20 kV and a 100 nA beam current. Th, U and Pb were
338 analysed concurrently with PET crystals using Mα lines for Th and Mβ lines for Pb
339 and U. The standards used were huttonite (Th), UO_2 and a synthetic Pb glass. The full
340 range of elements which are typically partitioned into monazite were analysed.
341 Offline corrections were made to account for the overlap of the second order Ce Lα
342 escape peak with the required Pb Mβ peak (Pyle et al., 2005), the overlap of the Th
343 Mγ peak on U Mβ and U Mz_2 on Pb Mβ. The ages for each spot were then
344 determined using the U-Th-Pb concentrations, and the statistical methods outlined in
345 Montel et al. (1996). Probe performance was monitored by comparison with a 514 Ma
346 monazite standard (MAD-1) with known U-Th-Pb concentrations. Reproducibility of

347 the standard during the course of the analytical sessions (n = 245) was 518 ± 5 Ma
348 (2σ; MSWD 0.98).
349
350 *6.2. SHRIMP Analytical techniques*
351
352 Selected samples were crushed and sieved to retrieve the <250 μm fraction. The
353 heavy mineral fraction was concentrated by panning and standard magnetic and
354 density methods to obtain a near pure sample. Individual titanite and monazite grains
355 were then hand picked under a binocular microscope and mounted in an epoxy disk
356 along with standard titanite and monazite crystals. The epoxy discs were then polished
357 and all titanite and monazite grains were BSE imaged using a Phillips XL20 SEM at
358 Adelaide Microscopy, in the University of Adelaide.
359 U-Pb isotopic measurements were carried out using the SHRIMP-II at the John de
360 Laeter Centre for Mass Spectrometry, Curtin University of Technology. Analytical
361 procedures for monazite analyses followed those outlined in Foster et al. (2000). The
362 primary oxygen ion beam produced a spot approximately 15 μm in diameter.
363 Monazite standard MAD-1 (514 Ma; $^{206}Pb/^{238}U = 0.0830$) was used to calibrate
364 $^{206}Pb/^{238}U$. Pb isotope ratios were corrected for minor common Pb based on
365 background-corrected ^{204}Pb counts, with the isotopic composition of the common Pb
366 component modelled upon that of 1700 Ma average crustal Pb (Stacey & Kramers,
367 1975). Normalisation of Pb/U ratios was based on a plot of ln($^{206}Pb/UO$) vrs UO_2/UO
368 for 10 analyses of the MAD-1 standard, which produced a calibration error of 5.90%
369 (2σ). Concordia plots (Tera & Wasserburg, 1972) and ages were produced using the
370 Isoplot/Ex v3.00 program of Ludwig (2003).

371 Analytical procedures for titanite analyses are similar to those outlined in Ireland
372 et al. (1990). The primary oxygen ion beam produced a spot approximately 35 μm in
373 diameter. Titanite standard Khan (518 ± 2 Ma; $^{206}Pb/^{238}U = 0.083671$) was used to
374 calibrate $^{206}Pb/^{238}U$. Pb isotope ratios were corrected for common Pb based on the
375 $^{208}Pb/^{206}Pb$ ratio with the isotopic composition of the common Pb component
376 modelled upon that of 1700 Ma average crustal Pb (Stacey & Kramers, 1975).
377 Normalisation of Pb/U ratios was based on a plot of $\ln(^{206}Pb/UO)$ vrs UO_2/UO for 11
378 analyses of the Khan standard, which produced a calibration error of 2.50% (2σ).
379
380 *6.3. U-Pb Geochronology Results*
381
382 EPMA chemical dating was done 'in situ' within thinsections, preserving the
383 textural relationships between monazite and the rock fabric. All analysed monazites
384 were located within the fabric and not as inclusions within porphyroblastic minerals.
385 Monazite EPMA chemical geochronological results range from 1691 Ma to 1736 Ma
386 (Table 3, fig. 7) and are consistent with those obtained from SHRIMP isotopic
387 methods. Due to the spread of ages and relatively large errors no difference in age
388 could be discerned between the migmatitic and mylonitic shear zones.
389 SHRIMP monazite U-Pb geochronology was undertaken on two shear zones: one
390 mylonitic adjacent to one of the metabasite intrusions (sample 2/05-11; fig. 4) and the
391 other was a wide migmatitic shear zone on the south coast of the Coffin Bay
392 Peninsula (sample SB 17; fig. 4). All monazites analysed were between 100 and 50
393 μm in size and pale greenish in colour. Textural relationships showed that the
394 monazite contained in the rock is within the foliation, and not included within
395 porphyroblastic phases. Thirty-two analyses of monazite from sample 2/05-11 (fig. 4)

were concordant or near concordant and combine to produced a $^{207}Pb/^{206}Pb$ weighted average age of 1725 ± 2 Ma (MSWD 1.8; Table 4, fig, 8). Twenty-five analyses of monazite from sample SB17 (fig. 4) were concordant or near concordant and combine to produced a $^{207}Pb/^{206}Pb$ weighted average age of 1721 ± 3 Ma (MSWD = 1.2; Table 4, fig. 8).

Titanite U-Pb ages come from metabasic dykes which contain a peak assemblage of hbd – pl – cpx – grt – qtz. Texturally the dated titanites form part of this peak assemblage. Due to the low concentrations of U and Pb in the titanite grains, individual spot errors are large (Table 5, fig. 8); however, all data are concordant or near concordant and combine to produce statistically meaningful concordia ages. Sample A2020 (n=19) produced a U-Pb concordia age of 1712 ± 8 Ma (MSWD 0.12). Sample SB32 (n=13) produced a concordant age of 1708 ± 12 Ma (MSWD 6.6).

6.4. Interpretation of geochronological results

Recent experimental data on the diffusivity of Pb in monazite suggests that for a 10 μm diameter grain, the Pb closure temperature (T_c) is in excess of 900°C at a cooling rate of 10°C/Ma (Cherniak et al., 2004). However, in migmatitic rocks it is likely that monazite stability, rather than closure temperature, will determine the age of monazite grains (Pyle & Spear, 2003).

The stability of monazite in melt-bearing peraluminous systems depends on a number of factors including the solubility of P and LREE (Pyle & Spear, 2003). Experimental monazite solubility data, determined as the total LREE content of granitic liquid, suggest that monazite solubility decreases with increasing Al content of the melt (Rapp & Watson, 1986; Wolf & London, 1995). However, experimental

421 evidence shows that the solubility of P in melt is also a function of the Al content in
422 the melt (Gan & Hess, 1992; Pichavant et al., 1992). In peraluminous melts, P
423 solubility increases to form $AlPO_4$ complexes, lowering the activity of P and therefore
424 destabilising phosphate phases (Pyle & Spear, 2003). Given that there is no evidence
425 of inheritance in the shear zone monazite, it is likely that all original monazite
426 dissolved, and that the monazite ages in the migmatitic shear zone sample corresponds
427 approximately to the timing of melt crystallisation.
428 The SHRIMP monazite age obtained from the mylonitic shear zones is identical to
429 that of the migmatitic shear zones. This suggests that monazite in the mylonitic shear
430 zones recrystallised (probably via a combination of dissolution and re-precipitation
431 and solid state recrystallisation) at the same time as monazite growth in the melt-
432 bearing shear zones. In this case, the simplest interpretation is that non-migmatitic
433 shear zones represent fluid poor structural equilivents of the migmatitic shear zones.
434 The EPMA monazite ages come from both migmatitic and mylonitic shear zone
435 samples. The resolution of these ages are too coarse to be able to interpret different
436 monazite growth events from this data. The above observations are consistent with the
437 observed similarities in the orientations of both the migmatitic and mylonitic shear
438 zones and the lack of any evidence for overprinting relationships.
439 Estimates of the T_c for U-Pb diffusion in titanite vary from c. 500°C up to >
440 700°C (Gascoyne, 1986; Scott & St-Onge, 1995; Zhang & Schaerer, 1996). However,
441 recent estimates have placed the T_c at approximately 660°C for grains with a 100 μm
442 radius of diffusion at a cooling rate of 10°C/Ma and a T_c of about 700°C for a cooling
443 rate of 100°C/Ma (Frost et al., 2000). The dated titanite grains range in size between
444 200 and 50 μm. It therefore seems likely that the titanite ages record closure of the
445 isotopic system slightly post-peak metamorphism (ie. <730°C). The differing T_c for

446 Pb diffusion between monazite and titanite provides an explanation for the offset in
447 the U-Pb ages obtained from the two accessory minerals in this study.
448
449 **8. Discussion**
450
451 EPMA monazite and SHRIMP U Pb monazite and titanate geochronology indicate
452 that mylonitic and migmatitic shear zones on the Coffin Bay Peninsula developed
453 during the Kimban Orogeny (c. 1730 - 1700 Ma). Peak metamorphic conditions
454 recorded in deformed and metamorphosed mafic intrusions indicate lower crustal
455 granulitic conditions (10 kbar at 730°C) occurred during this event. This was followed
456 by a period of near isothermal decompression producing pl – hbd coronas around grt –
457 cpx (e.g. Harley, 1989; Mawby et al., 1999; Zhao et al., 2000) and calculated
458 metamorphic conditions of 6-7 kbar at c. 700°C.
459 A major hindrance in determining a detailed evaluation of the larger-scale
460 interplay between deformation and metamorphism in the south-western Eyre
461 Peninsula is the paucity of outcrop. Importantly it makes determining a mechanism
462 for exhuming the lower crustal rocks speculative. Limited structural data suggest that
463 the migmatitic and mylonitic shear zones developed in a regionally dextral, top to the
464 NE deformational system. These shear zones were later deformed by a regional scale
465 tight easterly verging fold system which lead to the apparently conflicting kinematics
466 now seen in the shear zone system. There are no direct constraints on the timing of
467 this folding event except that it must post-date the development of the shear zones. K-
468 Ar data obtained from biotite and muscovite from the Four Hummocks and Coles
469 Point (fig. 2) indicate that the region had cooled through ~ 400°C (Hames & Bowring,
470 1994) by c. 1650 Ma (Webb et al., 1982). That these ages have not been reset during a

471 later event suggest that the folding occurred late in the Kimban Orogeny and not as a
472 discreet, later event.
473 Previous Rb-Sr (Nebel et al., 2007), K-Ar and Ar-Ar (Foster & Ehlers, 1998;
474 Webb et al., 1982) geochronology together with the geochronology presented here
475 allow us to interpret a temperature time path for the western Eyre Peninsula (fig. 9).
476 Following rapid decompression, cooling from peak and retrograde temperatures of
477 around 730 °C at 1720 Ma to c. 660 °C at 1710 Ma (recorded by the T_c of titanite)
478 occurred at a rate of about 8 $°CMa^{-1}$. This was followed by cooling at a rate of about 4
479 $°CMa^{-1}$ to 300 °C at c. 1620 Ma (fig. 9). This, when combined with the metamorphic
480 constraints discussed above, suggests the region underwent an initial near isothermal
481 decompression from 10 kbar to c. 6 kbar during the Kimban Orogeny, associated with
482 the development of the shear zone system and regional folding. This was then
483 followed by 100 Myr of slow cooling (fig. 9)
484 Decompression from 10 kbar to 6 kbar indicates approximately 12 km of uplift.
485 On the Coffin Bay Peninsula there are no structures of sufficient size to accommodate
486 this amount of vertical movement. Regional TMI data (fig. 10) indicate a large
487 regional scale structure, defined by a steep change from highly magnetic rocks to the
488 west and the magnetically bland rocks of the central Eyre Peninsula. This structure
489 runs between the high-grade rocks of the Coffin Bay Peninsula and the low-grade c.
490 1760 Ma Price Metasediments (Oliver & Fanning, 1997), which form a prominent
491 Kimban aged synclinal fold immediately to the east of the Coffin Bay region (fig. 2,
492 10). This curvi-linear structure is best discerned in the TMI image to the south of the
493 coast line, away from the dominating high magnetic response of the Price
494 Metasediments, and in part parallels the interpreted fold axis seen on the Coffin Bay
495 Peninsula. It is interpreted to be this structure which juxtaposes the lower crustal

496 rocks of the Coffin Bay Peninsula against the upper-crustal Price Metasediments
497 (Oliver & Fanning, 1997; Swain et al., 2005b; Teale et al., 2000) during the Kimban
498 Orogeny.
499 The tectonic system proposed here is similar to that proposed for the eastern Eyre
500 Peninsula where the Kimban Orogen is dominated by the dextrally transpressive
501 Kalinjala Shear Zone (Parker, 1993; Vassallo & Wilson, 2001; Vassallo & Wilson,
502 2002), which exhumed lower crustal granulites within the high strain belt (fig. 2). P-T
503 conditions reached 10 kbar and 750°C (Tong et al., 2004). Sm-Nd garnet-hornblende-
504 whole rock geochronology suggests this metamorphic peak was reached at 1730 ± 20
505 Ma (Hand et al., 1995). To the west of the Kalinjala Shear Zone the degree of
506 exhumation appears to decrease dramatically (Parker et al., 1993; Hand et al., 1995).
507 The variation in metamorphic grade across the Eyre Peninsula implies that the
508 upper crustal domain, represented by the Price Metasediments, is bounded on both
509 sides by domains with steep exhumation gradients, culminating in the exposure of
510 lower crustal rocks (fig. 10). In the case of the Kalinjala Shear Zone, geophysical data
511 of Thiel et al. (2005) indicates the transpressional shear zone is sub-vertical to at least
512 25 km, implying that exhumation was probably driven by translation along the shear
513 zone rather than across it (e.g. Goscombe et al., 2005; Goscombe et al., 2003). In the
514 case of the shear fabrics developed on the Coffin Bay Peninsula, and the interpreted
515 major structure seen in the TMI, their geometry at depth is unknown.
516
517 **9. Conclusion**
518
519 EPMA monazite and SHRIMP monazite and titanate geochronology indicate
520 that a series of predominantly N-NE trending migmatitic and mylonitic shear zones

developed on the Coffin Bay Peninsula between 1725 and 1700 Ma during the Kimban Orogeny. Granulite facies metamorphism at this time is recorded in deformed and metamorphosed mafic dykes, which intrude the peraluminous granites of the peninsula. This was followed by near isothermal decompression during the exhumation and juxtaposition of these lower-crustal rocks against the upper-crustal Price Metasediments along a regional scale interpreted shear system. This tectonic system in part reflects the development of the Kalinjala Shear system on the eastern Eyre Peninsula, which also exhumed lower-crustal rocks along a dextrally transpressive regional shear system.

Acknowledgements

The Authors would like to thank Anthony Reid, David Kelsey and two anonymous reviewers for constructive reviews on this paper. Primary Industries and Resources, South Australia is thanked for logistical support. J Payne and M Szpunar are thanked for assistance during fieldwork. Funding for this study has been provided by Australian Research Council Grant LP 0454301.

References

Betts, P. G. & Giles, D., 2006. The 1800-1100 Ma tectonic evolution of Australia. *Precambrian Research*, **144**(1-2), 92-125.

Cherniak, D. J., Watson, E. B., Grove, M. & Harrison, T. M., 2004. Pb diffusion in monazite: a combined RBS/SIMS study. *Geochimica et Cosmochimica Acta*, **68**(4), 829-840.

Daly, S. J. & Fanning, C. M., 1993. Archaean. In: *The geology of South Australia; Volume 1, The Precambrian.* (eds Drexel, J. F., Preiss, W. V. & Parker, A. J.) *Bulletin 54- Geological Survey of South Australia*, pp. 32-49.

549 Daly, S. J., Fanning, C. M. & Fairclough, M. C., 1998. Tectonic evolution and
550 exploration potential of the Gawler Craton, South Australia. *AGSO Journal of*
551 *Australian Geology and Geophysics*, **17**(3), 145-168.
552 Fanning, C. M., Flint, R. B., Parker, A. J., Ludwig, K. R. & Blissett, A. H., 1988.
553 Refined Proterozoic evolution of the Gawler Craton, South Australia, through
554 U-Pb zircon geochronology. *Precambrian Research*, **40/41**, 363-386.
555 Fanning, C. M., Oliver, R. L. & Cooper, J. A., 1981. The Carnot Gneisses,
556 southernmost Eyre Peninsula. *geological Survey of South Australia, Quarterly*
557 *Geological Notes*, **80**, 7-12.
558 Fanning, C. M., Reid, A. J. & Teale, G. S., 2007. A Geochronological framework for
559 the Gawler Craton, South Australia. *South Australia Geological Survey,*
560 *Bulletin*, **55**.
561 Ferris, G., Schwarz, M. & Heithersay, P., 2002. The Geological Framework,
562 Distribution and Controls of Fe-Oxide and Related Alteration, and Cu-Au
563 Mineralisation in the Gawler Craton, South Australia: Part 1: Geological and
564 Tectonic Framework. In: *Hydrothermal Iron Oxide Copper-Gold & Related*
565 *Deposits: A Global Perspective* (ed Porter, T.), PGC Publishing, Adelaide.
566 Foster, D. A. & Ehlers, K., 1998. ^{40}Ar-^{39}Ar thermochronology of the southern Gawler
567 Craton, Australia: Implications for Mesoproterozoic and Neoproterozoic
568 tectonics of East Gondwana and Rodinia. *Journal of Geophysical Research*,
569 **103**(B5), 10177-10193.
570 Foster, G., Kinny, P., Vance, D., Prince, C. & Harris, N., 2000. The significance of
571 monazite U-Th-Pb age data in metamorphic assemblages; a combined study of
572 monazite and garnet chronometry. *Earth and Planetary Science Letters*,
573 **181**(3), 327-340.
574 Frost, B. R., Chamberlain, K. R. & Schumacher, J. C., 2000. Sphene (titanite): phase
575 relations and role as a geochronometer. *Chemical Geology*, **172**, 131-148.
576 Gan, H. & Hess, P. C., 1992. Phosphate speciation in potassium aluminosilicate
577 glasses. *American Mineralogist*, **77**, 495-506.
578 Gascoyne, M., 1986. Evidence for the stability of potential nuclear waste host,
579 sphene, over geological time, from uranium-lead ages and uranium series
580 disequilibrium measurements. *Applied Geochemistry*, **1**, 199-210.
581 Giles, D., Betts, P. G. & Lister, G. S., 2004. 1.8-1.5-Ga links between the North and
582 South Australian Cratons and the Early-Middle Proterozoic configuration of
583 Australia. *Tectonophysics*, **380**, 27-41.
584 Goscombe, B., Gray, D. & Hand, M., 2005. Extrusional tectonics in the core of a
585 transpressional orogen; the Kaoko Belt, Namibia. *Journal of Petrology*, **46**(6),
586 1203-1241.
587 Goscombe, B., Hand, M., Gray, D. & Mawby, J., 2003. The metamorphic architecture
588 of a transpressional orogen: the Kaoko Belt, Namibia. *Journal of Petrology*,
589 **44**(4), 679-711.
590 Goscombe, B. & Trouw, R., 1999. The geometry of folded tectonic shear sense
591 indicators. *Journal of Structural Geology*, **21**, 123-127.
592 Hames, W. E. & Bowring, S. A., 1994. An Empirical-Evaluation of the Argon
593 Diffusion Geometry in Muscovite. *Earth and Planetary Science Letters*,
594 **124**(1-4), 161-167.
595 Hand, M., Bendall, B. R. & Sandiford, M., 1995. Metamorphic evidence for
596 Palaeoproterozoic oblique convergence in the eastern Gawler Craton.
597 *Geological Society of Australia, Abstracts*, **40**, 59.

598 Harley, S. L., 1989. The origins of granulites: a metamorphic perspective. *Geological*
599 *Magazine*, **126**, 215-247.
600 Holland, T. J. B. & Powell, R., 1998. An internally consistent dataset for phases of
601 petrological interest. *Journal of Metamorphic Geology*, **16**, 309-343.
602 Ireland, T. R., Compston, W., Williams, I. S. & Wendt, I., 1990. U-Th-Pb systematics
603 of individual perovslite grains from the Allende and Murchison carbonaceous
604 chondrites. *Earth and Planetary Science Letters*, **101**, 379-387.
605 Jagodzinski, E., frew, R., Foudoulis, C., Black, L. P., Reid, A., Zang, W., Payne, J. &
606 Schwarz, M., 2006. Compilation of SHRIMP U-Pb geochronological data for
607 the Gawler Craton, South Australia, 2006. *South Australia. Department of*
608 *Primary Industries and Resources. Report Book*, **2006/20**.
609 Ludwig, K. R., 2003. Users Manual for Isoplot/Ex, Version 3.00, A Geochronological
610 Toolkit for Microsoft Excel, Berkeley Geochronology Centre, Berkeley, CA,
611 2003. Special Publication No.4.
612 Mawby, J., Hand, M. & Foden, J., 1999. Sm-Nd evidence for high-grade Ordovician
613 metamorphism in the Arunta Block, central Australia. *Journal of Metamorphic*
614 *Geology*, **17**(6), 653-668.
615 Montel, J. M., Foret, S., Veschambre, M., Nicollet, C. & Provost, A., 1996. Electron
616 microprobe dating of monazite. *Chemical Geology*, **131**, 37-53.
617 Nebel, O., Nebel-Jacobsen, Y., Mezger, K. & Berndt, J., 2007. Initial Hf isotope
618 compositions in magmatic zircon from early Proterozoic rocks from the
619 Gawler Craton, Australia: a test for zircon model ages. *Chemical Geology*,
620 **doi: 10.1016/j.chemgeo.2007.02.008**.
621 Oliver, R. L. & Fanning, C. M., 1997. Australia and Antarctica; precise correlation of
622 Palaeoproterozoic terrains. In: *The Antarctic region; geological evolution and*
623 *processes; proceedings of the VII international symposium on Antarctic earth*
624 *sciences.* (ed C.A, R.) *International Symposium on Antarctic Earth Sciences*,
625 pp. 163-172, Terra Antarctica Publication, Siena, Italy.
626 Parker, A. J., 1980. The Kalinjala mylonite zone, eastern Eyre Peninsula.
627 Parker, A. J., 1993. Palaeoproterozoic. In: *The geology of South Australia; Volume 1,*
628 *The Precambrian.* (eds Drexel, J. F., Preiss, W. V. & Parker, A. J.) *Bulletin*
629 *54- Geological Survey of South Australia*, pp. 50-105.
630 Parrish, R. R., 1990. U-Pb dating of monazite and its application to geological
631 problems. *Canadian Journal of Earth Sciences*, **27**(11), 1431-1450.
632 Pattison, D. R. M., 2003. Petrogenic significance of orthopyroxene-free garnet +
633 clinopyroxene + plagioclase ± quartz-bearing metabasites with respect to the
634 amphibolite and granulite facies. *Journal of Metamorphic Geology*, **21**, 21-34.
635 Pichavant, M., Montel, J. M. & Richard, L. R., 1992. Apatite solubilitu in
636 peraluminous liquids: Experimental data and an extension of the Harrison-
637 Watson model. *Geochemica et Cosmochimica Acta*, **56**, 3855-3861.
638 Powell, R. & Holland, T. J. B., 1988. An internally consistent dataset with
639 uncertainties and correlations; 3, Applications to geobarometry, worked
640 examples and a computer program. *Journal of Metamorphic Geology*, **6**(2),
641 173-204.
642 Pyle, J. M. & Spear, F. S., 2003. Four generations of accessory-phase growth in low-
643 pressure migmatites from SW New Hampshire. *American Mineralogist*, **88**,
644 338-351.
645 Pyle, J. M., Spear, F. S., Wark, D. A., Daniel, C. G. & Storm, L. C., 2005.
646 Contributions to precission and accuracy of monazite microprobe ages.
647 *American Mineralogist*, **90**, 547-577.

Rapp, R. P. & Watson, E. B., 1986. Monazite solubility and dissolution kinetics: implications for the thorium and light rare earth chemistry of felsic magmas. *Contributions to Mineralogy and Petrology*, **94**, 304-316.

Reid, A., Vassallo, J. J., Wilson, C. J. L. & Fanning, C. M., 2007. Timing of the Kimban Orogen on the southern Eyre Peninsula. *South Australia. Department of Primary Industries and Resources. Report Book*, **2007/5**.

Schwarz, M., 2003a. Lincoln, South Australia, explanatory notes: 1:250000 geological series, sheet SI53-11. *Geological Survey of South Australia*.

Schwarz, M. P., 2003b. LINCOLN Map Sheet. *South Australia. Geological Survey. Geological Atlas 1:250,000 Series (Sheet SH53-11)*.

Scott, D. J. & St-Onge, M. R., 1995. Constraints on Pb closure temperature in titanite based on rocks from the Ungava orogen, Canada; implications for U-Pb geochronology and P-T-t path determinations. *Geology*, **23**, 1123-1126.

Spear, F. S., 1993. *Metamorphic phase equilibria and pressure-temperature-time paths*. Mineralogical Society of America, Washington, D.C.

Stacey, J. S. & Kramers, J. D., 1975. Approximation of terrestrial lead isotope evolution by a two-stage model. *Earth and Planetary Science Letters*, **26**(2), 207-221.

Swain, G., Hand, M., Teasdale, J., Rutherford, L. & Clark, C., 2005a. Age constraints on terrane-scale shear zones in the Gawler Craton, southern Australia. *Precambrian Research*, **139**, 164-180.

Swain, G., Woodhouse, A., Hand, M., Barovich, K., Schwarz, M. & Fanning, C. M., 2005b. Provenance and tectonic development of the late Archaean Gawler Craton, Australia; U-Pb zircon, geochemical and Sm-Nd isotopic implications. *Precambrian Research*, **141**, 106-136.

Teale, G. S., Schwarz, M. & Fanning, C. M., 2000. Potential for Archaean VHMS-style mineralisation and other targets in southern Eyre Peninsula. *Mines and Energy South Australia Journal*, **18**, 17-21.

Tera, F. & Wasserburg, G. J., 1972. U-Th-Pb systematics in three Apollo 14 basalts and the problem of initial Pb in lunar rocks. *Earth and Planetary Science Letters*, **14**(3), 281-304.

Thiel, S., Heinson, G. & White, A., 2005. Tectonic evolution of the southern Gawler Craton, South Australia, from electromagnetic sounding. *Australian Journal of Earth Sciences*, **52**, 887-896.

Thomson, B. P., 1980. *Geological map of South Australia*. Geol. Surv. South Australia, Dep. Mines Energy, Adelaide, Australia.

Tong, L., Wilson, C. J. L. & Vassallo, J. J., 2004. Metamorphic evolution and reworking of the Sleaford Complex metapelites in the southern Eyre Peninsula, South Australia. *Australian Journal of Earth Sciences*, **51**(4), 571-589.

Vassallo, J. J. & Wilson, C. J. L., 2001. Structural repetition of the Hutchison Group metasediments, Eyre Peninsula, South Australia. *Australian Journal of Earth Sciences*, **48**(2), 331-345.

Vassallo, J. J. & Wilson, C. J. L., 2002. Palaeoproterozoic regional-scale non-coaxial deformation; an example from eastern Eyre Peninsula, South Australia. *Journal of Structural Geology*, **24**(1), 1-24.

Wade, B. P., Barovich, K. M., Hand, M., Scrimgeour, I. R. & Close, D. F., 2006. Evidence for early Mesoproterozoic arc magmatism in the Musgrave Block, central Australia; implications for Proterozoic crustal growth and tectonic reconstructions of Australia. *Journal of Geology*, **114**(1), 43-63.

Webb, A. W., Thomson, B. P., Blisset, A. H., Daly, J. S., Flint, R. B. & Parker, A. J., 1982. Geochronology of the Gawler Craton, South Australia. *Department of Primary Industries and Resources, South Australia*, **Report Book 82/86**, 136.

Webb, A. W., Thomson, B. P., Blissett, A. H., Daly, S. J., Flint, R. B. & Parker, A. J., 1986. Geochronology of the Gawler Craton, South Australia. *Australian Journal of Earth Sciences*, **33**(2), 119-143.

Williams, M. L. & Jercinovic, M. J., 2002. Microprobe monazite geochronology; putting absolute time into microstructural analysis. *Journal of Structural Geology*, **24**, 1013-1028.

Wolf, M. B. & London, D., 1995. Incongruent dissolution of REE- and Sr-rich apatite in peraluminous granitic liquids: differential apatite, monazite and xnenotime solubilities during anatexis. *American Mineralogist*, **80**, 765-775.

Wolf, M. B. & Wyllie, P. J., 1994. Dehydration melting of amphibole at 10kbar; the effects of temperature and time. *Contributions to Mineralogy and Petrology*, **115**(4), 369-383.

Zhang, L. S. & Schaerer, U., 1996. Inherited Pb components in magmatic titanite and their consequence for the interpretation of U-Pb ages. *Earth and Planetary Science Letters*, **138**, 1-4.

Zhao, G. C., Wilde, S. A., Cawood, P. A. & Lu, L. Z., 2000. Petrology and P-T path of the Fruping mafic granulites: implications for tectonic evolution of teh central zone of the North China Craton. *Journal of Metamorphic Geology*, **18**, 375-391.

Figure Captions

fig. 1. Simplified interpreted subsurface geology of the Gawler Craton, South Australia (modified from: Daly et al., 1998; Ferris et al., 2002, Swain et al., 2005a)

fig. 2. Interpreted sub-surface geology of the Eyre Peninsula overlain on the TMI image (modified from Schwarz, 2003b). Shown are the locations of the Price Metasediments and Hall Bay Volcanics together with the outcrop locations of the Wangary Gneiss at Frenchmans and Coles Point.

fig. 3. (a) Photo of garnet – cordierite – tabular K- feldspar granite with weak magmatic flow frabric defined by weakly aligned feldspar grains, orientated roughly left to right. (b) Photo of typical Coffin Bay outcrop with an outcropping mafic dyke in the foreground. (c) Photomicrograph of andalusite stable schist from Coles Point.

735 (d) Asymmetric flow pertabation folds in a migmatitic felsic shear zone on the south
736 coast indicating sinistral shear sense. (e) Photo of a felsic mylonitc shear zone from
737 the south coast of the Coffin Bay Peninsula. (f) Garnet bearing mafic shear zone with
738 plagioclase + hornblende coronas defining the foliation. (g) Migmatitic shear zone
739 with fabric concordant, cross cutting and shear band felsic leucosomes. (h) Garnet –
740 clinopyroxene bearing felsic melts crosscutting the hornblende foliation in a deformed
741 mafic dyke.
742
743 fig. 4. Structural Map of the Coffin Bay Peninsula. The asymmetry of the foliation
744 data (which define a girdle on the equal area stereonets) and the opposing kinematics
745 on either side of the peninsula suggest the shear zones are folded in an east-vergent
746 fold system. (a) Schematic drawing of shear zone formation in a regionally dextral
747 transpressional setting followed by (b) tight east-verging folding producing the
748 apparent opposing kinematics now seen (e.g. Goscombe and Trouw, 1999). PT
749 locations correspond to Table 2. Geochronology samples are indicated by sample
750 name and [1] EPMA monazite, [2] SHRIMP titanite and [3] SHRIMP monazite.
751
752 fig. 5. (a) Photomicrograph of felsic grt – sill – ksp – pl – qtz ± bi assemblage used for
753 PT calculations (abbreviations after Kretz, 1983). (b) Peak mafic assemblage of grt –
754 cpx – pl – hbd_1 – qtz. (c) Post peak assemblage where grt + cpx have almost
755 completely reacted out to form a pl + hbd_2 pseudomorph. The foliation wraps the pl +
756 hbd_2 (fomer grt) pseudomorph suggesting deformation was syn to post
757 metamorphism.
758

fig. 6. (SB 31) Quantitative garnet cation profile across an unretrogressed mafic garnet. The profile still maintains a slight bell shape curve in spessartine recording the prograde growth of garnet. (SB 4) Typical mafic garnet cation profile for the Coffin Bay metabasites with flat profile indicating equilibration at peak conditions.

fig. 7. Relative probability histograms for EPMA monazite geochronology. Sample numbers correspond to locations in fig. 4.

fig. 8. (a-b) Tera-Wasserburg U-Pb concordia diagrams for titanite SHRIMP data from metabasic dykes; sample locations correlate to fig. 4. (c-d) Tera-Wasserburg U-Pb concordia diagrams for monazite SHRIMP data from felsic shear zones; sample locations correlate to fig. 4

fig. 9. Temperature – time diagram for the western Eyre Peninsula. Peak PT from thermobarometry at 1720 Ma. Initial cooling from peak conditions to the T_c of titanate (at 1710 Ma) occurred at c. 8 °CMa^{-1} followed by slow cooling at c. 4 °CMa^{-1} to 1600 Ma.

fig. 10. TMI image of the Eyre Peninsula (same area as in fig. 2). Arrows show bulk kinematics for both the Coffin Bay Peninsula and the Kalinjala Shear Zone. Schematic Cross-section A-A` demonstrates the intense variation in metamorphic pressures across the Eyre Peninsula as a result of the Kimban Orogen (CB Coffin Bay, PM Price Metasediments, KSZ Kalinjala Shear Zone).

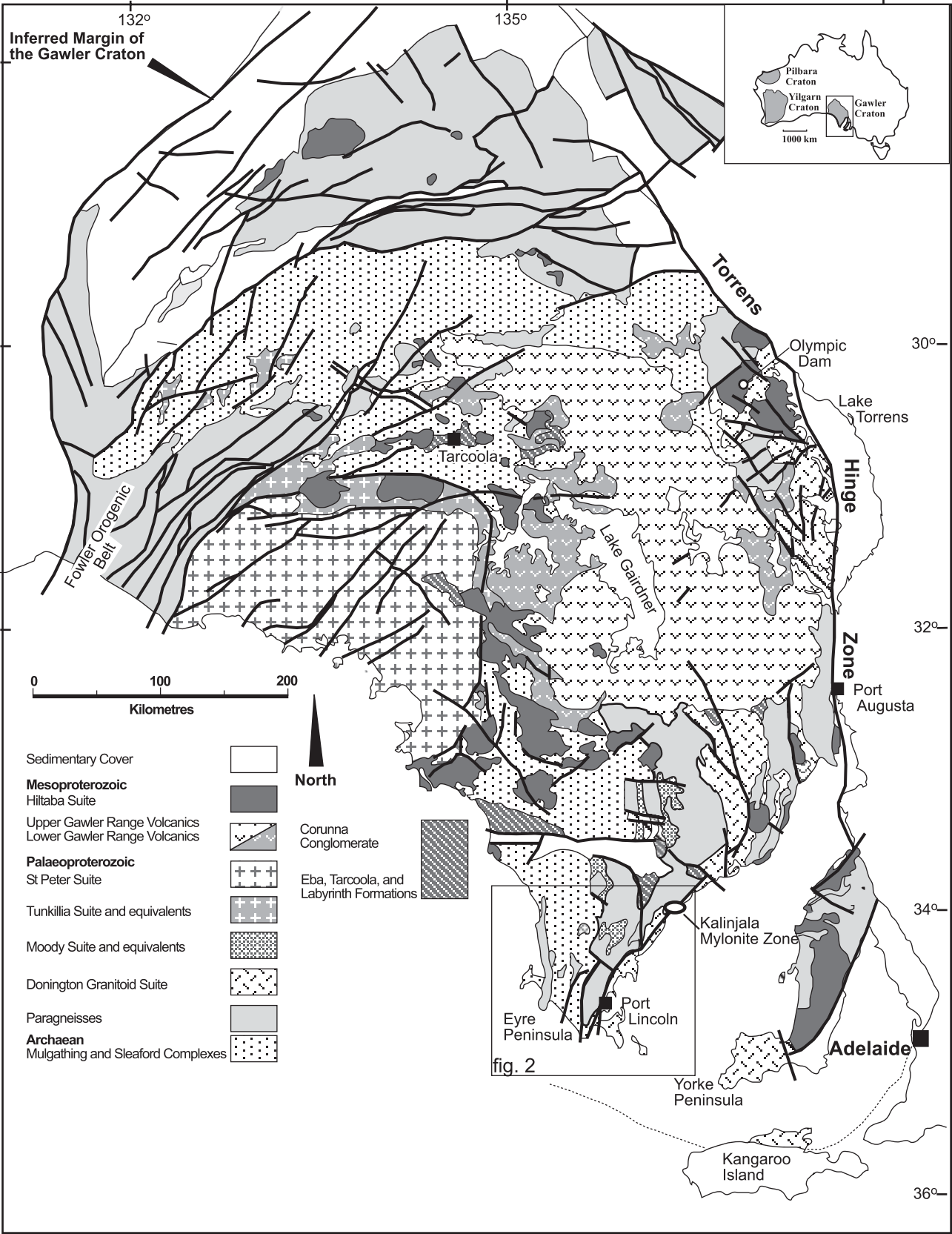
132°
135°
Inferred Margin of the Gawler Craton
Pilbara Craton
Yilgarn Craton
Gawler Craton
1000 km
Torrens
Olympic Dam
30°
Lake Torrens
Hinge
Zone
Tarcoola
Lake Gairdner
Fowler Orogenic Belt
32°
Port Augusta
0
100
200
Kilometres
North
Sedimentary Cover
Mesoproterozoic
Hiltaba Suite
Upper Gawler Range Volcanics
Lower Gawler Range Volcanics
Palaeoproterozoic
St Peter Suite
Tunkillia Suite and equivalents
Moody Suite and equivalents
Donington Granitoid Suite
Paragneisses
Archaean
Mulgathing and Sleaford Complexes
Corunna Conglomerate
Eba, Tarcoola, and Labyrinth Formations
Kalinjala Mylonite Zone
34°
Port Lincoln
Eyre Peninsula
fig. 2
Adelaide
Yorke Peninsula
Kangaroo Island
36°

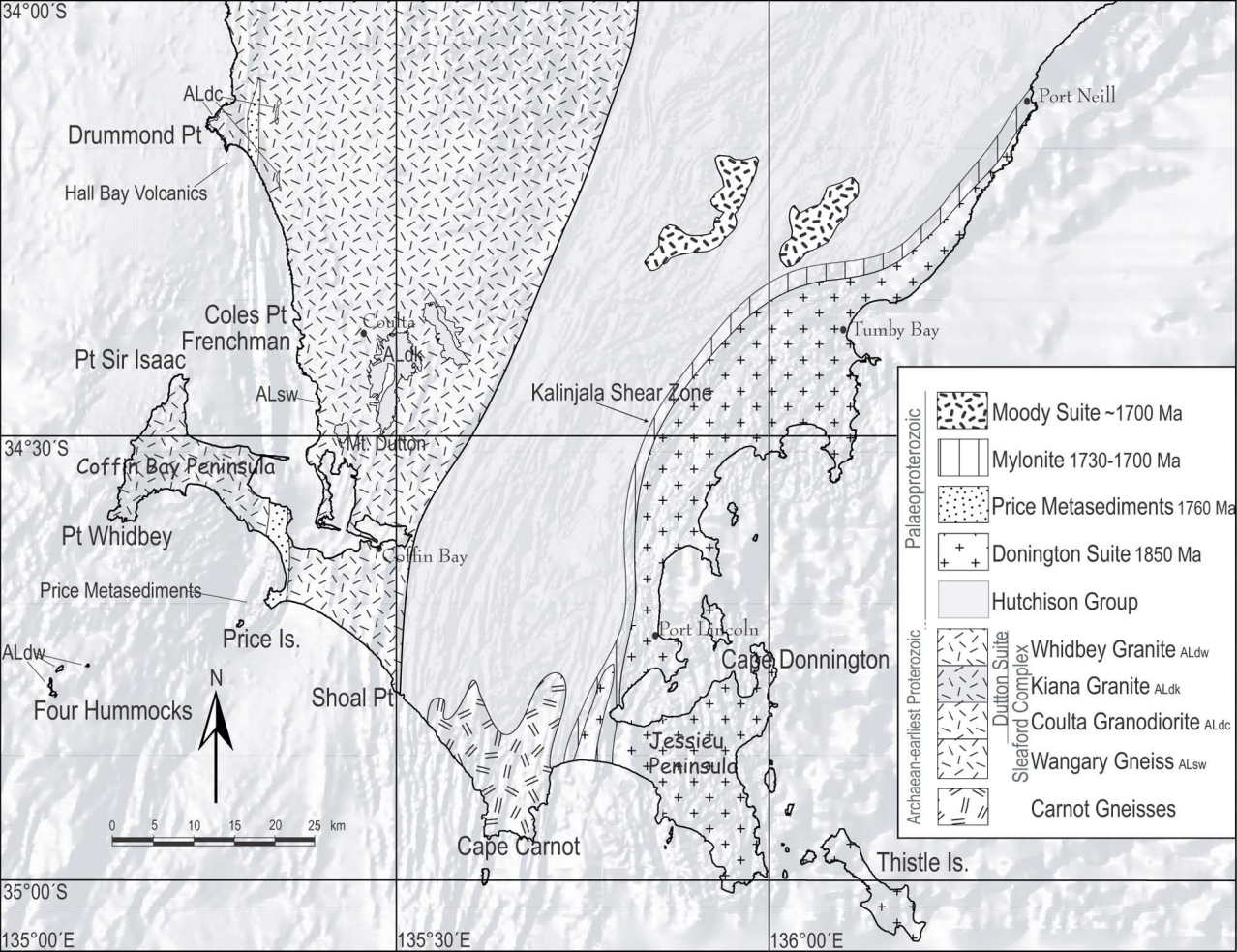
34°00´S
34°30´S
35°00´S
135°00´E
135°30´E
136°00´E
ALdc
Drummond Pt
Hall Bay Volcanics
Coles Pt
Frenchman
Pt Sir Isaac
ALsw
Coulta
ALdk
Mt Dutton
Coffin Bay Peninsula
Pt Whidbey
Coffin Bay
Price Metasediments
Price Is.
ALdw
Four Hummocks
Shoal Pt
N
0 5 10 15 20 25 km
Kalinjala Shear Zone
Port Neill
Tumby Bay
Port Lincoln
Cape Donnington
Jessieu Peninsula
Cape Carnot
Thistle Is.
Palaeoproterozoic
Moody Suite ~1700 Ma
Mylonite 1730-1700 Ma
Price Metasediments 1760 Ma
Donington Suite 1850 Ma
Hutchison Group
Archaean-earliest Proterozoic
Dutton Suite
Sleaford Complex
Whidbey Granite ALdw
Kiana Granite ALdk
Coulta Granodiorite ALdc
Wangary Gneiss ALsw
Carnot Gneisses


a


b

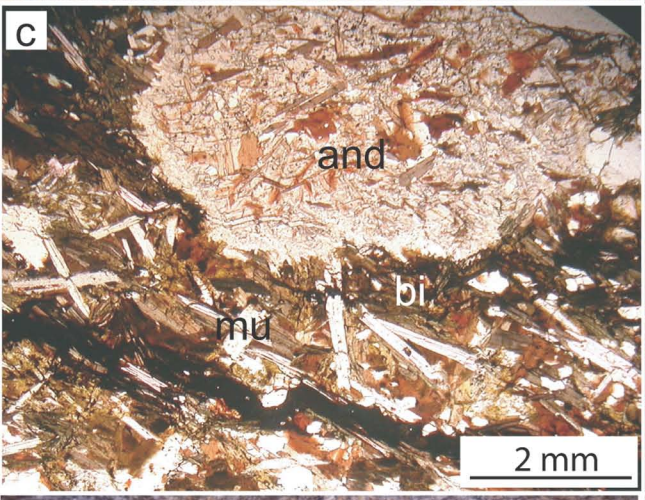
c
and
bi
mu
2 mm

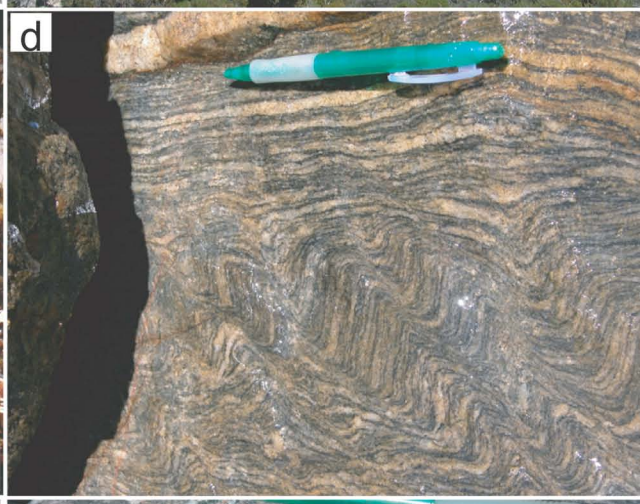
d

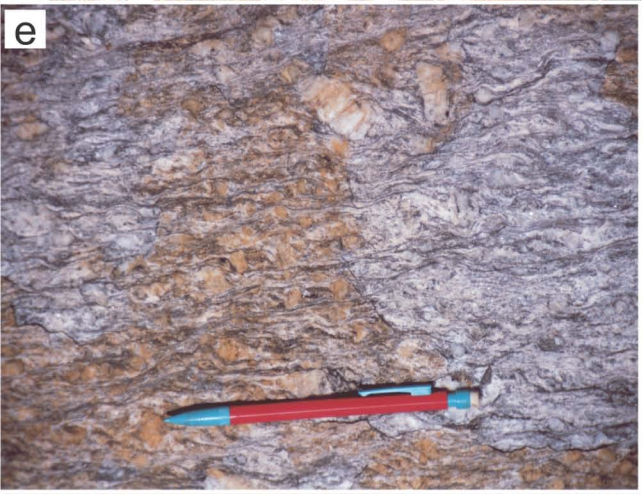
e


f


g


h

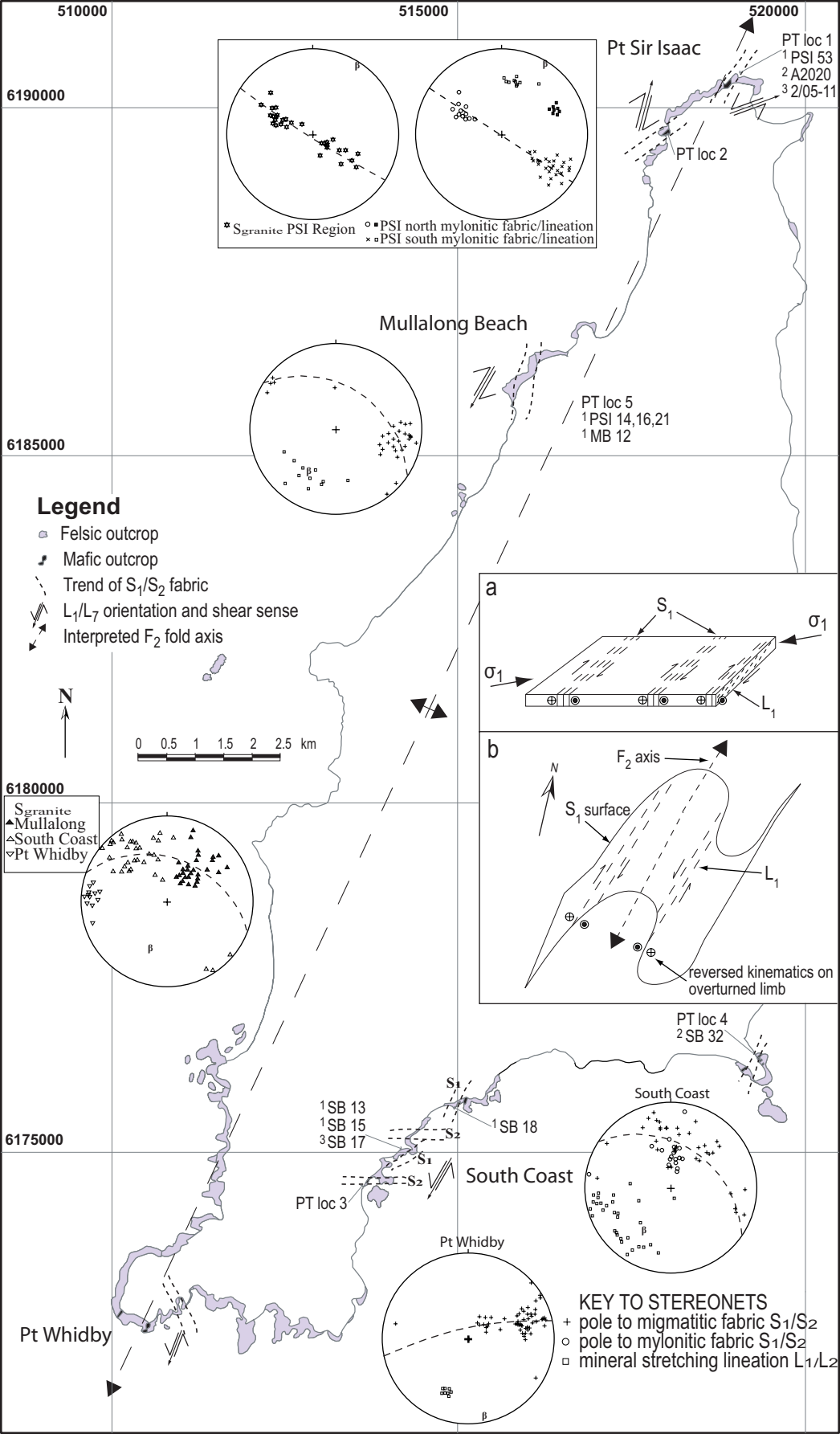
510000
515000
520000
6190000
6185000
6180000
6175000
Pt Sir Isaac
PT loc 1
1 PSI 53
2 A2020
3 2/05-11
PT loc 2
Sgranite PSI Region
PSI north mylonitic fabric/lineation
PSI south mylonitic fabric/lineation
Mullalong Beach
PT loc 5
1 PSI 14,16,21
1 MB 12
Legend
Felsic outcrop
Mafic outcrop
Trend of S1/S2 fabric
L1/L7 orientation and shear sense
Interpreted F2 fold axis
N
0 0.5 1 1.5 2 2.5 km
a
S1
σ1
σ1
L1
b
F2 axis
N
S1 surface
L1
reversed kinematics on overturned limb
Sgranite
Mullalong
South Coast
Pt Whidby
PT loc 4
2 SB 32
S1
1 SB 13
1 SB 15
3 SB 17
S2
1 SB 18
S1
S2
PT loc 3
South Coast
South Coast
Pt Whidby
Pt Whidby
KEY TO STEREONETS
+ pole to migmatitic fabric S1/S2
○ pole to mylonitic fabric S1/S2
□ mineral stretching lineation L1/L2

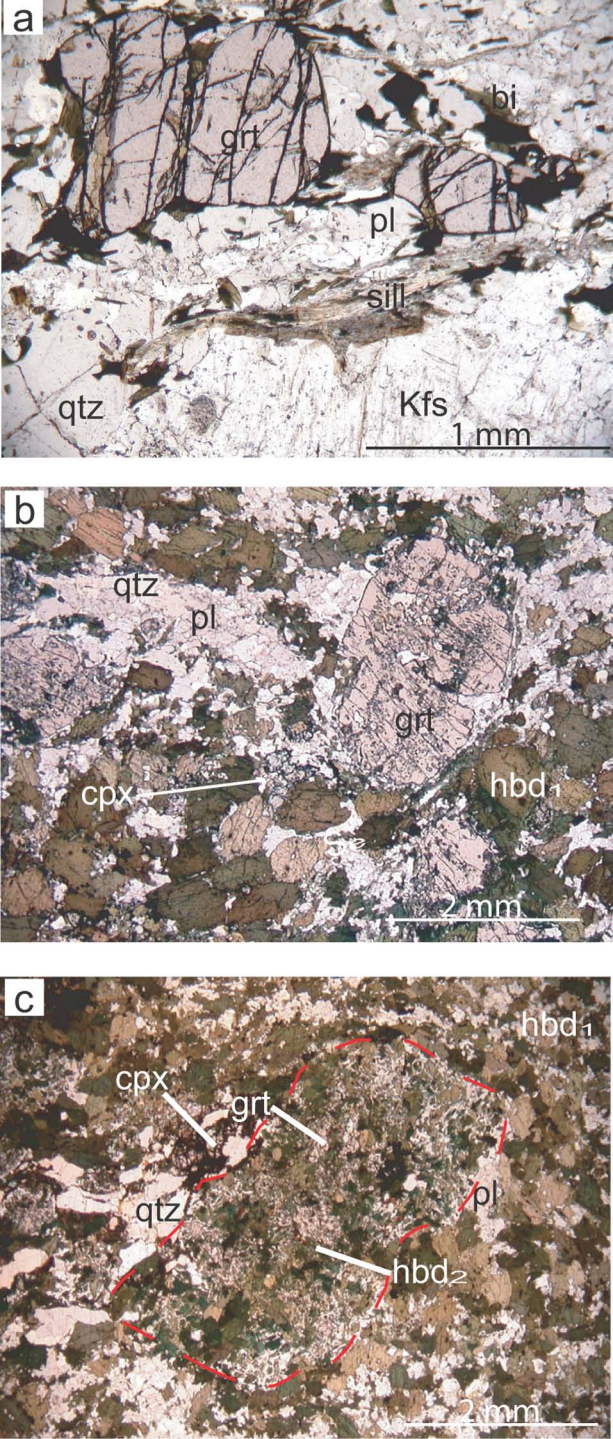
a
bi
grt
pl
sill
qtz
Kfs
1 mm
b
qtz
pl
grt
cpx
hbd1
2 mm
c
hbd1
cpx
grt
qtz
pl
hbd2
2 mm

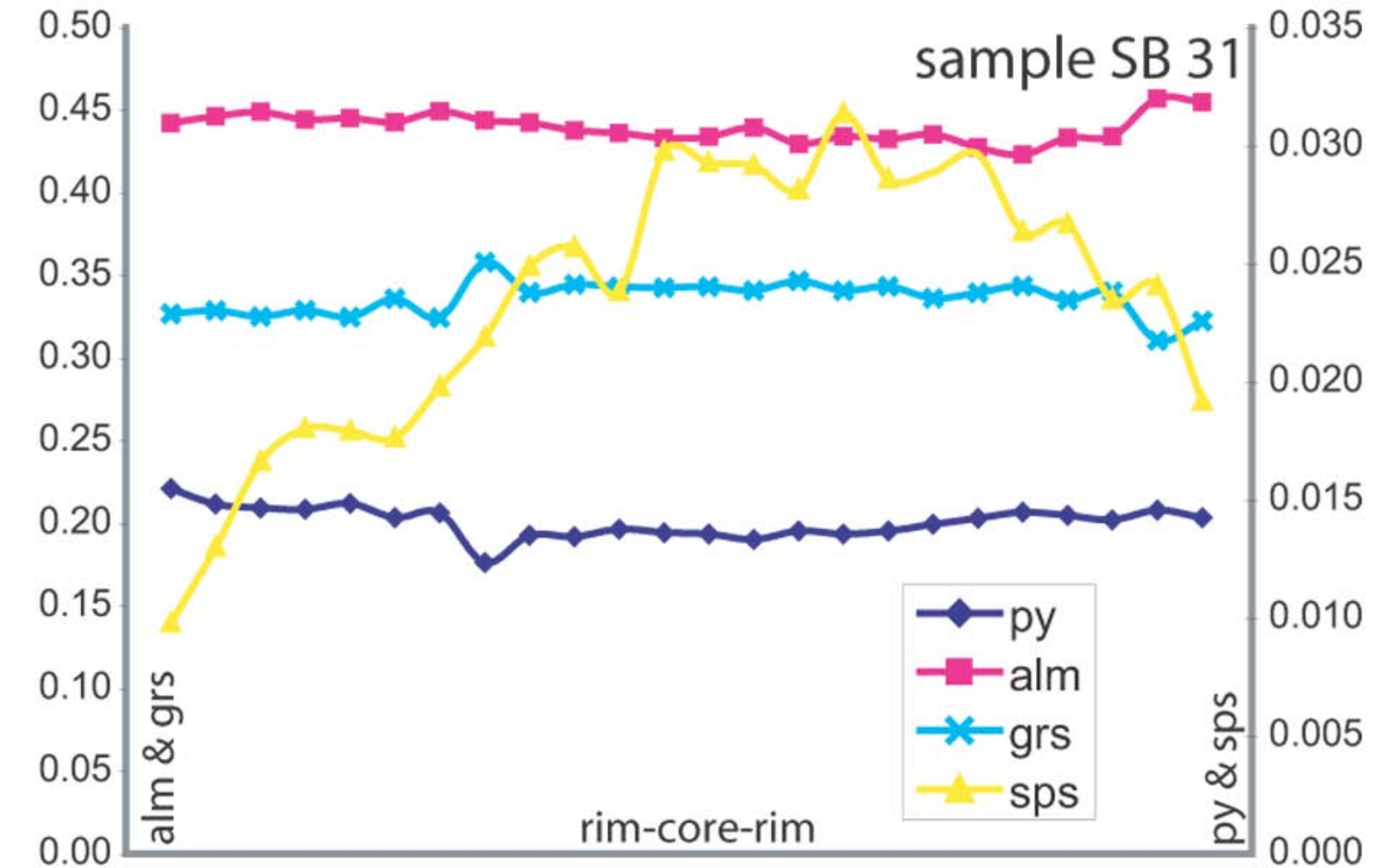
sample SB 31
0.50
0.45
0.40
0.35
0.30
0.25
0.20
0.15
0.10
0.05
0.00
0.035
0.030
0.025
0.020
0.015
0.010
0.005
0.000
alm & grs
rim-core-rim
py & sps
py
alm
grs
sps

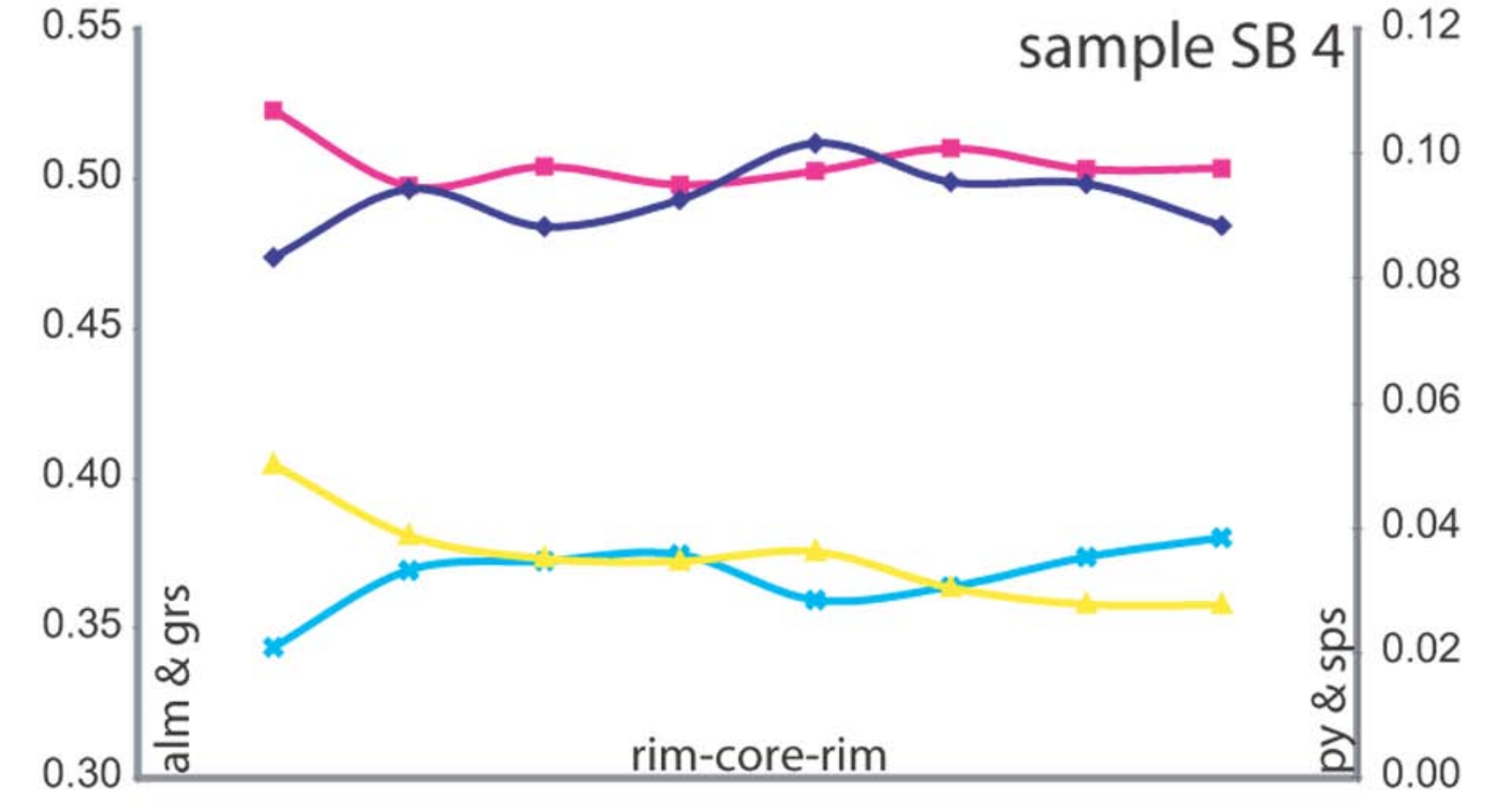
sample SB 4
0.55
0.50
0.45
0.40
0.35
0.30
0.12
0.10
0.08
0.06
0.04
0.02
0.00
alm & grs
rim-core-rim
py & sps

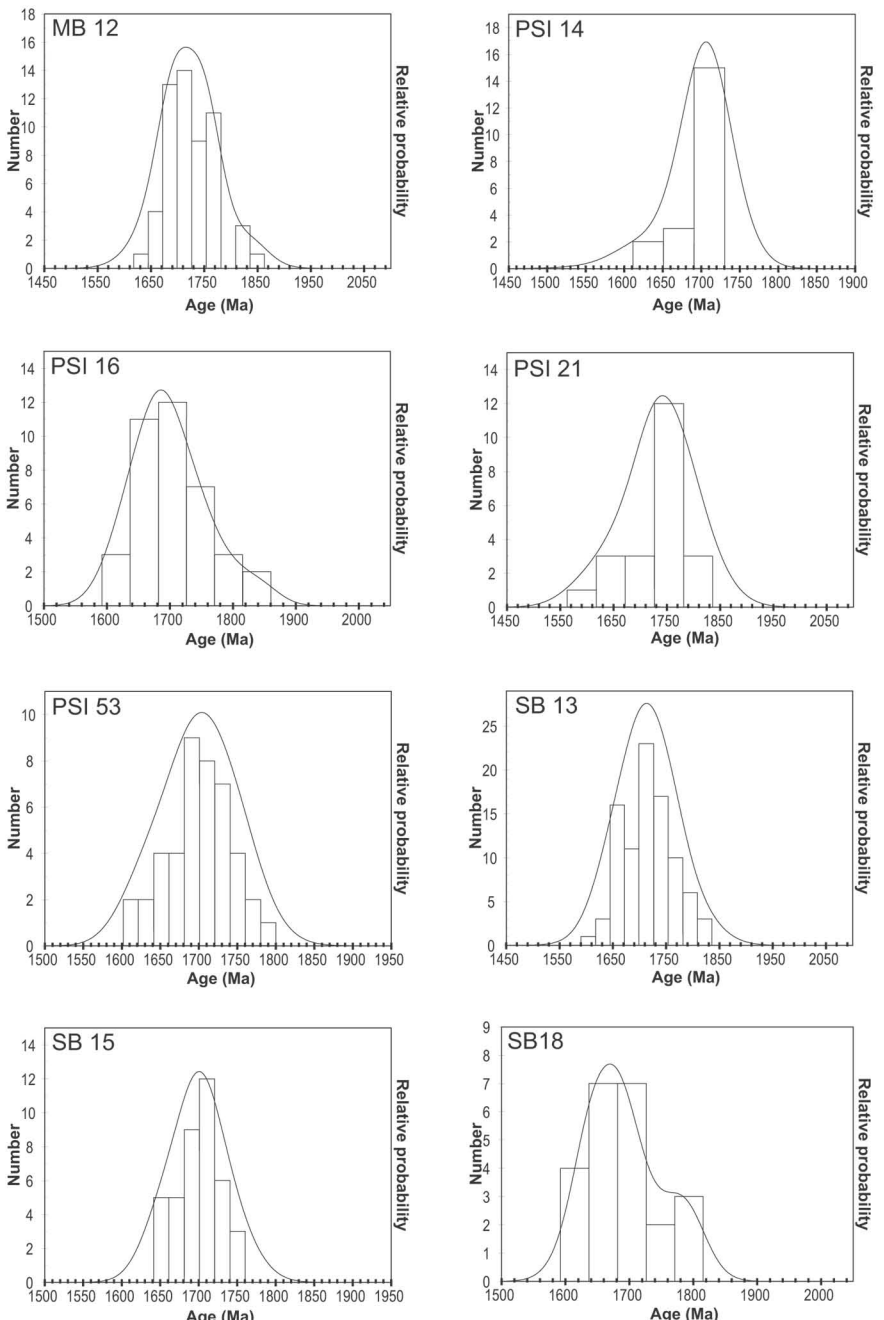
MB 12
PSI 14
PSI 16
PSI 21
PSI 53
SB 13
SB 15
SB18
Number
Relative probability
Age (Ma)

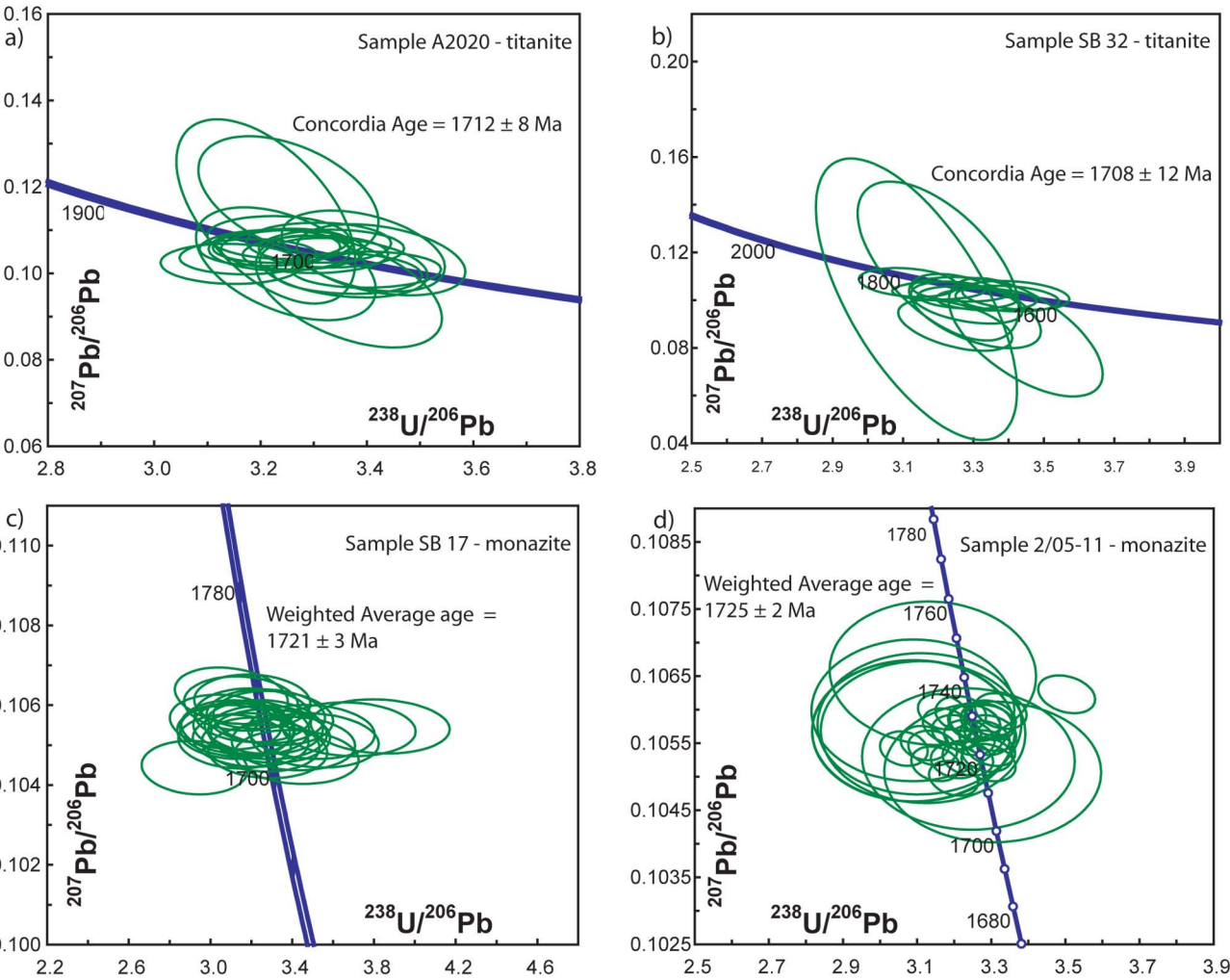
a)
Sample A2020 - titanite
Concordia Age = 1712 ± 8 Ma
1900
1700
$^{207}Pb/^{206}Pb$
$^{238}U/^{206}Pb$
b)
Sample SB 32 - titanite
Concordia Age = 1708 ± 12 Ma
2000
1800
1600
$^{207}Pb/^{206}Pb$
$^{238}U/^{206}Pb$
c)
Sample SB 17 - monazite
1780
Weighted Average age =
1721 ± 3 Ma
1700
$^{207}Pb/^{206}Pb$
$^{238}U/^{206}Pb$
d)
Sample 2/05-11 - monazite
1780
Weighted Average age =
1725 ± 2 Ma
1760
1740
1720
1700
1680
$^{207}Pb/^{206}Pb$
$^{238}U/^{206}Pb$

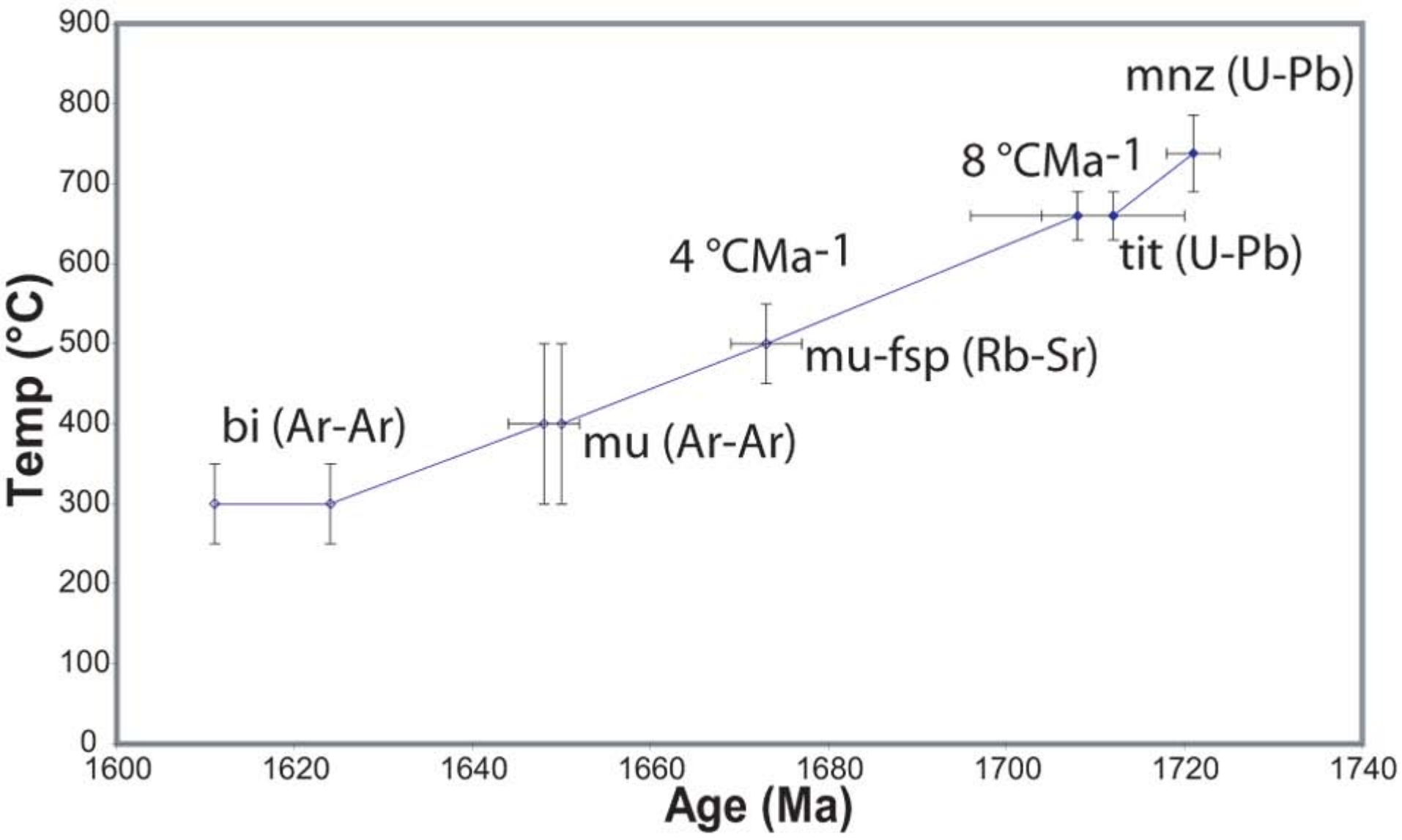
900
800
700
600
500
400
300
200
100
0
Temp (°C)
1600
1620
1640
1660
1680
1700
1720
1740
Age (Ma)
mnz (U-Pb)
8 °CMa-1
tit (U-Pb)
4 °CMa-1
mu-fsp (Rb-Sr)
bi (Ar-Ar)
mu (Ar-Ar)

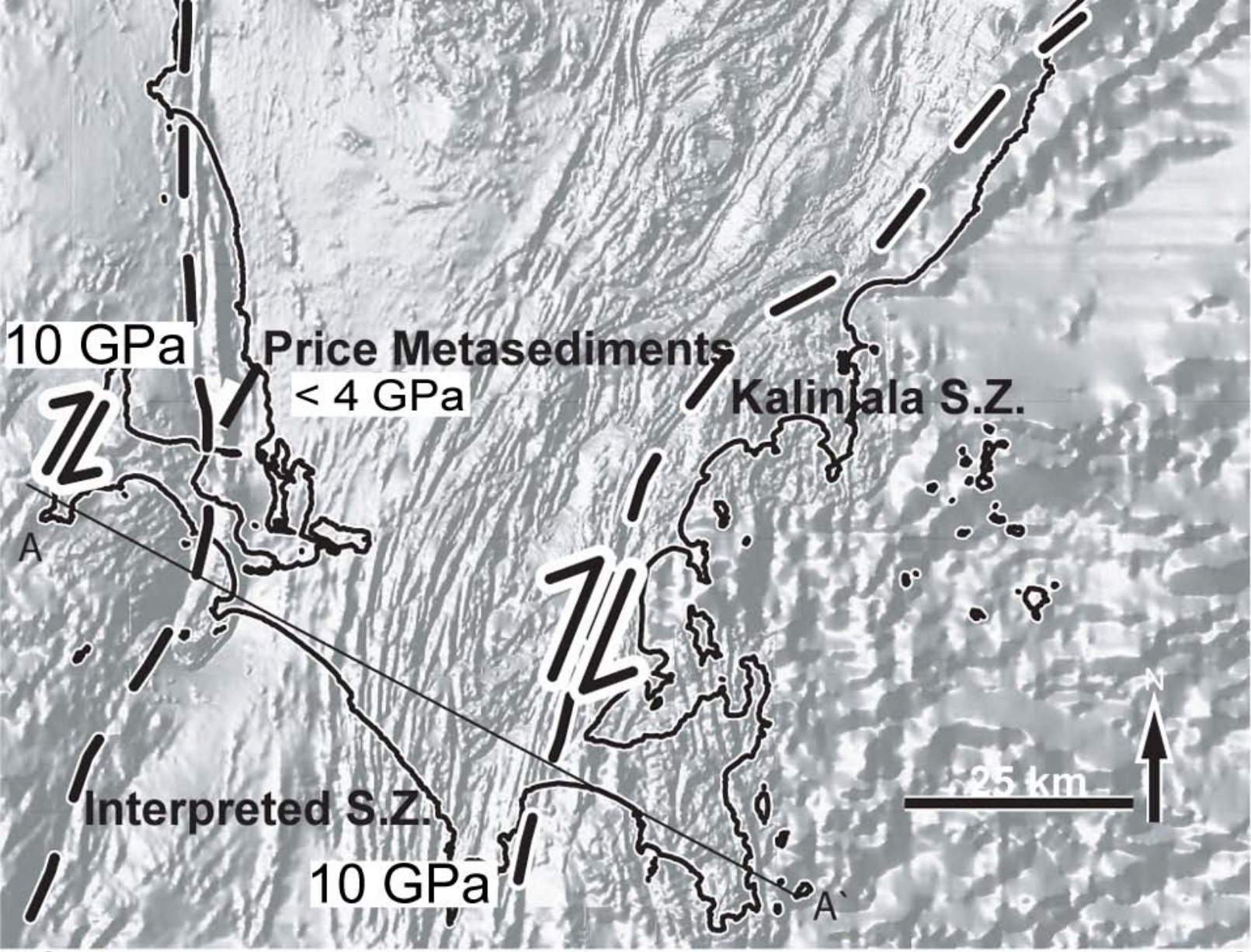
10 GPa
Price Metasediments
< 4 GPa
Kalinjala S.Z.
A
Interpreted S.Z.
10 GPa
A`
N
25 km

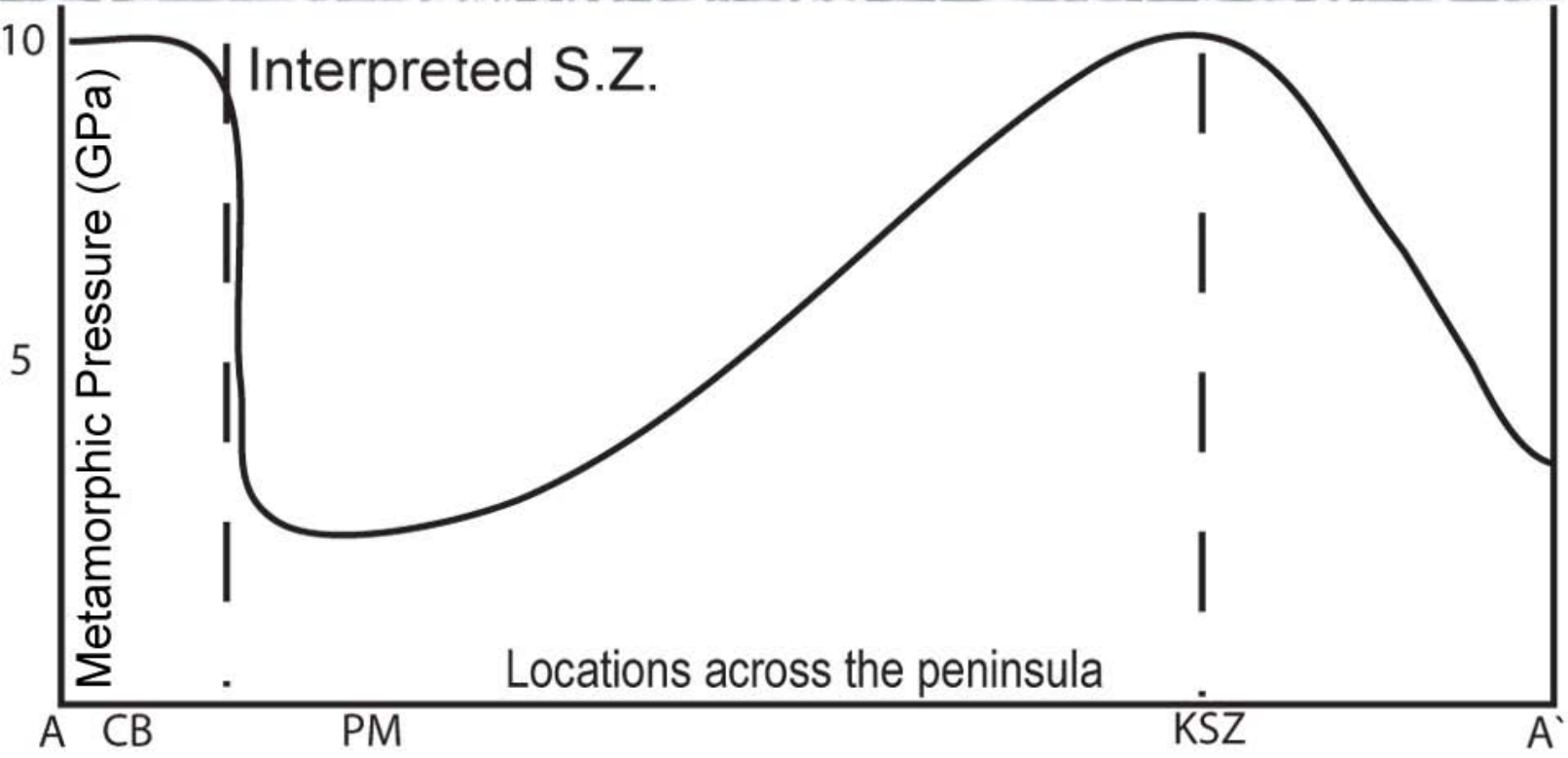
10
5
Metamorphic Pressure (GPa)
Interpreted S.Z.
Locations across the peninsula
A
CB
PM
KSZ
A`

Table 1

Representative mineral analyses from selected Coffin Bay metabasites

Sample	PSI 38					SB 10					SB 6			MB 12			
Mineral	Grt core	Grt rim	Amph	Pl	Ilm	Grt core	Grt rim	Amph	Pl	Cpx	Grt	Amph	Pl	Grt core	Grt rim	Bi	Ksp
SiO_2	38.47	37.92	42.88	60.55	0.13	38.56	38.44	42.33	53.75	52.364	38.22	41.30	52.61	36.60	36.66	31.57	65.41
TiO_2	0.11	0.29	1.28	0.03	48.45	0.17	0.00	1.01	0.00	0.092	0.10	0.77	0.04	0.00	0.00	0.95	0.00
Al_2O_3	21.14	21.00	12.40	24.34	0.00	21.32	21.33	11.53	28.79	2.0246	21.18	11.33	29.59	20.85	20.45	18.33	18.78
Cr_2O_3	0.06	0.00	0.05	0.00	0.00	0.00	0.00	0.00	0.00	0.0276	0.00	0.03	0.00	0.04	0.00	0.03	0.00
FeO^T	23.71	23.56	18.58	0.16	43.87	23.34	22.76	20.93	0.42	10.0051	22.09	24.20	0.15	33.39	32.78	28.81	0.06
MnO	0.89	0.32	0.18	0.00	1.10	1.16	0.76	0.37	0.00	0.1263	0.89	0.60	0.01	5.57	6.82	0.68	0.05
MgO	2.69	2.93	9.02	0.01	0.00	2.51	2.68	7.15	0.01	11.6883	2.23	5.22	0.00	1.64	1.40	4.81	0.01
CaO	13.10	13.45	10.73	7.14	0.46	13.35	13.57	10.83	12.13	21.9439	15.21	11.10	12.75	0.58	0.72	0.00	0.04
Na_2O	0.03	0.02	1.55	6.84	0.00	0.01	0.05	1.51	4.21	0.6997	0.01	1.38	4.17	0.00	0.00	0.09	0.73
K_2O	0.01	0.01	0.83	0.31	0.00	0.02	0.01	0.73	0.11	0.023	0.00	0.71	0.07	0.00	0.00	6.94	15.66
Total	100.21	99.50	97.51	99.37	94.01	100.46	99.60	96.40	99.43	98.9945	99.93	96.64	99.39	98.68	98.84	92.21	100.73
Oxygens	24	24	23	32	6	24	24	23	32	6	24	23	32	24	24	22	32
Si	6.0262	5.9798	6.4738	10.8343	0.0035	6.0232	6.0356	6.5525	9.7708	1.98121	5.9991	6.5046	9.5919	6.0233	6.0463	5.2080	11.9688
Al^{IV}	0.0000	0.0202	1.5262	0.0000	0.0000	0.0000	0.0000	1.4475	0.0000	0.01879	0.0009	1.4954	0.0000	0.0000	0.0000	2.7920	0.0000
Al^{VI}	3.9025	3.8836	0.6802	5.1331	0.0000	3.9256	3.9468	0.6557	6.1677	0.07149	3.9178	0.6079	6.3573	4.0449	3.9746	0.7721	4.0497
Cr	0.0070	0.0000	0.0063	-	0.0000	0.0000	0.0000	0.0000	-	0.00083	0.0000	0.0037	-	0.0053	0.0000	0.0043	-
Fe^{3+}	0.0339	0.1146	-	0.0215	0.0413	0.0000	0.0000	-	0.0576	0	0.0951	-	0.0209	0.0000	0.0000	-	0.0000
Ti	0.0132	0.0343	0.1455	0.0034	0.9826	0.0198	0.0000	0.1175	0.0000	0.00262	0.0115	0.0916	0.0060	0.0000	0.0000	0.1176	0.0000
Mg	0.6285	0.6881	2.0310	0.0022	0.0000	0.5844	0.6279	1.6506	0.0030	0.65926	0.5226	1.2245	0.0001	0.4033	0.3447	1.1825	0.0025
Fe^{2+}	3.0723	2.9926	2.3460	0.0000	0.9479	3.0491	2.9887	2.7102	0.0000	0.31657	2.8049	3.1870	0.0000	4.5957	4.5212	3.9741	0.0087
Mn	0.1184	0.0430	0.0228	0.0000	0.0251	0.1537	0.1007	0.0490	0.0000	0.00405	0.1185	0.0803	0.0012	0.7760	0.9527	0.0947	0.0075
Ca	2.1983	2.2735	1.7356	1.3692	-	2.2349	2.2830	1.7971	2.3627	0.88958	2.5580	1.8729	2.4898	0.1031	0.1264	0.0000	0.0070
Na	0.0090	0.0058	0.4536	2.3725	-	0.0028	0.0147	0.45212	1.4847	0.05133	0.0034	0.4225	1.4749	0.0001	0.0011	0.0287	0.2607
K	0.0020	0.0028	0.1606	0.0698	-	0.0040	0.0020	0.1447	0.0249	0.00111	0.0000	0.1422	0.0169	0.0000	0.0000	1.4609	3.6545
OH	-	-	2.0000	-	-	-	-	2.0000	-	-	-	2.0000	-	-	-	4.0000	-
Sum	16.01	16.04	17.58	19.81	2.00	16.00	16.00	17.58	19.87	4.00	16.03	17.63	19.96	15.95	15.97	19.63	19.96

Sample PSI 38 from Pt Sir Isaac Section;SB 10 from Pt Whidby east section; SB 6 from Pt Whidby section, grt almost absent sample; Mb 12 Felsic shear zone sample (fig. 4)

^{T} total Fe, Fe^{3+} calculated via the method of Droop (1987)

Table 2
Summary of average P-T results from analysed metabasites

Location	Sample	Ave P	1σ error	Ave T	1σ error
Pt Sir Isaac	PSI 38 a	9.43	1.47	765	81
Peak	PSI 38 b	9.73	0.93	786	47
	PSI 43 a	9.16	0.95	827	64
	PSI 43 b	10.79	0.86	754	59
	PSI 35 a	10.22	1.13	719	74
	PSI 35 b	10.25	1.28	770	89
	PSI 45 b	10.5	0.86	734	42
Weighted ave		10.08	0.75*	763	44*
Pt Sir Isaac Sth	PSI 2 a	10.89	0.86	698	42
Peak	PSI 2 b	10.05	1.08	756	66
	PSI 5 a	10.29	0.99	752	67
	PSI 5 b	11.21	1.19	763	75
Weighted ave		10.61	0.99*	729	57*
Pt Whidby east	SB 2 a	10.1	1.15	761	65
Peak	SB 2 b	8.78	0.98	730	57
	SB 3 a	10.92	0.82	705	59
	SB 3 b	8.87	0.84	813	66
	SB 10 b	8.97	1.08	729	62
Weighted ave		9.58	0.83*	744	54*
Pt Whidby east	SB 4 b	7.64	1.11	723	68
Retrograde	SB 6 a	6.56	1.35	871	97
	SB 6 b	6.73	1.4	915	176
Weighted ave		7.1	1.4*	785	100*
Sensation Bch	Sb 30a	10.87	0.84	725	54
Peak	SB 31 a	11.2	0.87	707	51
	SB 31 b	10.89	1.07	791	65
	SB 32 a	9.78	0.81	705	44
	SB 32 b	10.43	1.01	677	48
Weighted ave		10.6	0.79*	713	45*

* errors at 95% confidence

Table 3
Summary of EPMA monazite geochronological results

Sample	Location	n	Wt % range			Age ± error (Ma)	
			Pb	Th	U	95% conf.	Wlsq ± 2σ (MSWD)
MB 12	Mull	56	0.46 - 1.5	3.2 - 13.13	0.51 - 1.62	1721 ± 12	1723 ± 12 (1.7)
PSI 14	Mull	19	0.43 - 1.50	3.52 - 16.56	0.16 - 1.19	1706 ± 8	1705 ± 14 (0.35)
PSI 16	Mull	38	0.48 - 1.39	6.16 - 11.38	0.71 - 1.53	1698 ± 18	1700 ± 18 (3.1)
PSI 21	Mull	22	0.34 - 0.87	3.78 - 7.66	0.25 - 1.23	1736 ± 25	1731 ± 24 (1.3)
PSI 53	PSI	43	0.3 - 1.51	3.62 - 14.4	0.07 - 1.5	1700 ± 14	1700 ± 14 (1.9)
SB 13	Sth Cst	90	0.27 - 1.47	4.28 - 14.77	0.15 - 1.00	1714 ± 10	1713 ± 9 (1.5)
SB 15	Sth Cst	42	0.29 - 1.64	3.62 - 16.87	0.12 - 1.12	1700 ± 9	1697 ± 9 (0.99)
SB 18	Sth Cst	23	0.79 - 1.45	7.86 - 15.44	0.46 - 1.5	1691 ± 25	1694 ± 25 (3.5)

Table 4
Monazite U-Pb SHRIMP isotopic data

Spot Label	Th/U	Common ^{206}Pb (%)	^{207}Pb/^{206}Pb	^{206}Pb/^{238}U	^{207}Pb/^{235}U	^{206}Pb/^{238}U age (Ma)	^{207}Pb/^{206}Pb age (Ma)	% conc
SB17.10a	18.5	0.01	0.105438 ± 0.000409	0.312535 ± 0.018297	4.543588 ± 0.268768	1753 ± 90	1722 ± 7	102
SB17.11a	8.9	0.01	0.105327 ± 0.000341	0.321242 ± 0.01878	4.665249 ± 0.275035	1796 ± 92	1720 ± 6	104
SB17.12a	7.4	0.02	0.105092 ± 0.000392	0.320639 ± 0.018764	4.64607 ± 0.274603	1793 ± 92	1716 ± 7	104
SB17.14a	10.1	0.01	0.105384 ± 0.000291	0.319667 ± 0.018701	4.644869 ± 0.273626	1788 ± 91	1721 ± 5	104
SB17.14b	9.9	0.02	0.105445 ± 0.000409	0.318997 ± 0.018671	4.637799 ± 0.27429	1785 ± 91	1722 ± 7	104
SB17.14c	11.1	0.00	0.105452 ± 0.000359	0.306664 ± 0.017938	4.458809 ± 0.263144	1724 ± 89	1722 ± 6	100
SB17.15a	14.8	0.28	0.104702 ± 0.000421	0.292265 ± 0.017119	4.219241 ± 0.249824	1653 ± 85	1709 ± 7	97
SB17.16a	12.6	0.00	0.105014 ± 0.000422	0.308103 ± 0.018028	4.461116 ± 0.263875	1731 ± 89	1715 ± 7	101
SB17.17a	22.4	0.00	0.105397 ± 0.000339	0.271877 ± 0.0159	3.950951 ± 0.232986	1550 ± 81	1721 ± 6	90
SB17.18a	10.6	0.03	0.105468 ± 0.000401	0.261038 ± 0.015281	3.795981 ± 0.224469	1495 ± 78	1722 ± 7	87
SB17.18b	11.2	0.09	0.105329 ± 0.000386	0.286202 ± 0.016746	4.156451 ± 0.24557	1623 ± 84	1720 ± 7	94
SB17.18c	12.0	0.01	0.105118 ± 0.000448	0.284815 ± 0.016714	4.128017 ± 0.24507	1616 ± 84	1716 ± 8	94
SB17.19a	9.5	0.01	0.105723 ± 0.000294	0.305747 ± 0.017879	4.456894 ± 0.262467	1720 ± 88	1727 ± 5	100
SB17.19b	11.9	0.00	0.10513 ± 0.000345	0.312823 ± 0.018297	4.534453 ± 0.267484	1755 ± 90	1717 ± 6	102
SB17.20a	11.9	0.02	0.105042 ± 0.000346	0.293605 ± 0.017174	4.252355 ± 0.250881	1660 ± 86	1715 ± 6	97
SB17.20b	11.5	0.02	0.105679 ± 0.000411	0.302406 ± 0.017695	4.40635 ± 0.260532	1703 ± 88	1726 ± 7	99
SB17.21a	10.5	0.11	0.105317 ± 0.000307	0.304969 ± 0.017834	4.428504 ± 0.260894	1716 ± 88	1720 ± 5	100
SB17.21b	11.4	0.11	0.105229 ± 0.0003	0.303651 ± 0.017771	4.405672 ± 0.259701	1709 ± 88	1718 ± 5	99
SB17.3a	10.6	0.03	0.106237 ± 0.000682	0.322368 ± 0.018972	4.722044 ± 0.283292	1801 ± 92	1736 ± 12	104
SB17.3b	11.3	0.08	0.104436 ± 0.000378	0.342205 ± 0.020037	4.927599 ± 0.291295	1897 ± 96	1704 ± 7	111
SB17.3c	19.1	0.04	0.10609 ± 0.000317	0.312081 ± 0.018258	4.565007 ± 0.269126	1751 ± 90	1733 ± 5	101
SB17.4a	9.9	0.17	0.105747 ± 0.000274	0.311812 ± 0.018228	4.546324 ± 0.267497	1750 ± 90	1727 ± 5	101
SB17.4b	13.6	0.09	0.10484 ± 0.000263	0.304784 ± 0.017819	4.405745 ± 0.259195	1715 ± 88	1712 ± 5	100
SB17.8	15.6	0.03	0.105579 ± 0.000508	0.325273 ± 0.019069	4.735085 ± 0.281349	1815 ± 93	1724 ± 9	105
SB17.9a	11.4	0.04	0.10604 ± 0.000353	0.317504 ± 0.01857	4.642157 ± 0.273867	1778 ± 91	1732 ± 6	103
11b.1a	8.6	0.05	0.105683 ± 0.000224	0.323602 ± 0.018915	4.715408 ± 0.277048	1807 ± 92	1726 ± 4	105
11b.1b	8.4	0.03	0.105683 ± 0.000286	0.323557 ± 0.018913	4.714722 ± 0.277481	1807 ± 92	1726 ± 5	105
11b.2a	6.7	0.02	0.105263 ± 0.000392	0.308783 ± 0.018058	4.48156 ± 0.264684	1735 ± 89	1719 ± 7	101
11b.2b	8.0	0.02	0.106541 ± 0.000449	0.318222 ± 0.018614	4.674636 ± 0.276584	1781 ± 91	1741 ± 8	102
11b.3b	10.0	0.01	0.104892 ± 0.000231	0.325978 ± 0.019052	4.71447 ± 0.277024	1819 ± 93	1712 ± 4	106
11b.3c	11.3	0.08	0.105664 ± 0.000361	0.320921 ± 0.018764	4.675472 ± 0.27583	1794 ± 92	1726 ± 6	104
11b.4a	5.6	0.02	0.10507 ± 0.00029	0.302665 ± 0.017691	4.384711 ± 0.25808	1705 ± 88	1716 ± 5	99

11b.4b	6.0	0.03	0.105788 ± 0.000207	0.321898 ± 0.018814	4.695205 ± 0.275718	1799 ± 92	1728 ± 4	104
11b.5	9.4	0.01	0.105988 ± 0.000243	0.323759 ± 0.01893	4.731309 ± 0.278197	1808 ± 92	1732 ± 4	104
11a-12a	10.7	0.02	0.105428 ± 0.000198	0.318259 ± 0.004408	4.626364 ± 0.065731	1781 ± 22	1722 ± 3	103
11a-13a	13.1	0.04	0.10533 ± 0.0002	0.304053 ± 0.004181	4.415738 ± 0.06232	1711 ± 21	1720 ± 3	99
11a-13b	15.6	0.03	0.105979 ± 0.000245	0.300702 ± 0.004167	4.393967 ± 0.062974	1695 ± 21	1731 ± 4	98
11a-15a	12.5	0.09	0.106227 ± 0.000283	0.285426 ± 0.004131	4.180537 ± 0.062873	1619 ± 21	1736 ± 5	93
11a-16a	9.4	0.16	0.10521 ± 0.000259	0.303702 ± 0.004447	4.405587 ± 0.066738	1710 ± 22	1718 ± 5	100
11a-16b	12.5	0.02	0.105964 ± 0.000244	0.315594 ± 0.004361	4.61095 ± 0.065888	1768 ± 21	1731 ± 4	102
11a-17a	10.8	0.02	0.10519 ± 0.000217	0.317468 ± 0.004362	4.604442 ± 0.065143	1777 ± 21	1718 ± 4	103
11a-18a	10.7	0.02	0.105802 ± 0.00024	0.307294 ± 0.004398	4.482802 ± 0.066202	1727 ± 22	1728 ± 4	100
11a-1a	11.8	0.11	0.105874 ± 0.000232	0.303259 ± 0.004183	4.426946 ± 0.063012	1707 ± 21	1730 ± 4	99
11a-1b	14.5	0.05	0.105577 ± 0.000204	0.304727 ± 0.004155	4.435913 ± 0.062142	1715 ± 21	1724 ± 4	99
11a-20a	7.0	0.01	0.10594 ± 0.000187	0.310776 ± 0.004351	4.539504 ± 0.065036	1745 ± 21	1731 ± 3	101
11a-21	8.6	0.01	0.105232 ± 0.000199	0.312101 ± 0.0043	4.528416 ± 0.064027	1751 ± 21	1718 ± 3	102
11a-22a	12.2	0.03	0.105663 ± 0.000206	0.311891 ± 0.00425	4.543878 ± 0.063629	1750 ± 21	1726 ± 4	101
11a-22b	11.6	0.04	0.105583 ± 0.000227	0.308549 ± 0.004277	4.491782 ± 0.064186	1734 ± 21	1724 ± 4	101
11a-5a	11.1	0.03	0.105808 ± 0.000216	0.307096 ± 0.004236	4.480155 ± 0.063591	1726 ± 21	1728 ± 4	100
11a-5b	11.3	0.02	0.105808 ± 0.000229	0.303466 ± 0.004176	4.427202 ± 0.062846	1708 ± 21	1728 ± 4	99
11a-6a	9.7	0.04	0.105276 ± 0.000224	0.308939 ± 0.004298	4.484371 ± 0.064283	1735 ± 21	1719 ± 4	101
11a-6b	9.7	0.02	0.104976 ± 0.000238	0.312638 ± 0.00428	4.525161 ± 0.064037	1754 ± 21	1714 ± 4	102
11a-7a	11.4	0.01	0.10565 ± 0.000232	0.303299 ± 0.004269	4.418151 ± 0.064124	1708 ± 21	1726 ± 4	99
11a-7b	12.1	0.18	0.105756 ± 0.000257	0.314374 ± 0.00427	4.584067 ± 0.064604	1762 ± 21	1727 ± 4	102
11a-8a	12.0	0.01	0.105832 ± 0.000218	0.30423 ± 0.004219	4.43934 ± 0.063355	1712 ± 21	1729 ± 4	99
11a-8b	11.9	0.04	0.105424 ± 0.000273	0.303376 ± 0.004145	4.409848 ± 0.062711	1708 ± 21	1722 ± 5	99
11a-9a	9.7	0.06	0.1055 ± 0.000189	0.320439 ± 0.004401	4.661204 ± 0.065591	1792 ± 21	1723 ± 3	104
11a-9b	10.6	0.00	0.105418 ± 0.000187	0.326349 ± 0.004516	4.743481 ± 0.067202	1821 ± 22	1722 ± 3	106

Table 5
Titanite U-Pb SHRIMP isotopic data

Spot Label	U (ppm)	Th (ppm)	Common ^{206}Pb (%)	^{207}Pb/^{206}Pb	^{206}Pb/^{238}U	^{207}Pb/^{235}U	^{206}Pb/^{238}U age (Ma)	^{207}Pb/^{206}Pb age (Ma)	% conc
2020.11	23	15	4	0.100853 ± 0.002388	0.294197 ± 0.008016	4.090997 ± 0.156559	1662 ± 40	1640 ± 44	101
2020.15	34	22	3	0.105907 ± 0.002246	0.310781 ± 0.008432	4.538187 ± 0.165489	1745 ± 41	1730 ± 39	101
2020.16	29	13	5	0.10385 ± 0.002182	0.314718 ± 0.008472	4.506387 ± 0.162933	1764 ± 42	1694 ± 39	104
2020.17	10	4	12	0.101318 ± 0.004916	0.297938 ± 0.009239	4.162092 ± 0.252877	1681 ± 46	1648 ± 90	102
2020.19	29	36	4	0.10531 ± 0.002966	0.309079 ± 0.008382	4.487867 ± 0.186109	1736 ± 41	1720 ± 52	101
2020.2	7	2	26	0.117957 ± 0.010229	0.307466 ± 0.010569	5.000579 ± 0.486019	1728 ± 52	1925 ± 156	90
2020.24	22	10	7	0.105452 ± 0.002753	0.306697 ± 0.008402	4.459299 ± 0.178964	1724 ± 41	1722 ± 48	100
2020.25	31	14	4	0.106375 ± 0.001946	0.308523 ± 0.008224	4.525079 ± 0.154591	1733 ± 41	1738 ± 34	100
2020.26	24	14	6	0.104381 ± 0.00246	0.302757 ± 0.00827	4.357295 ± 0.166622	1705 ± 41	1703 ± 43	100
2020.28	21	17	6	0.099945 ± 0.003006	0.297373 ± 0.008198	4.097908 ± 0.177307	1678 ± 41	1623 ± 56	103
2020.3	12	6	17	0.103157 ± 0.006039	0.291837 ± 0.008909	4.150867 ± 0.287769	1651 ± 44	1682 ± 108	98
2020.3.a	17	7	8	0.102196 ± 0.002871	0.317999 ± 0.00886	4.480848 ± 0.188056	1780 ± 43	1664 ± 52	107
2020.30.a	12	22	12	0.105162 ± 0.006938	0.294711 ± 0.008787	4.273253 ± 0.323558	1665 ± 44	1717 ± 122	97
2020.31	25	24	6	0.108297 ± 0.003143	0.309283 ± 0.008424	4.618205 ± 0.194949	1737 ± 41	1771 ± 53	98
2020.33	27	17	5	0.105721 ± 0.002526	0.299999 ± 0.008104	4.373048 ± 0.167206	1691 ± 40	1727 ± 44	98
2020.33.a	6	5	33	0.114331 ± 0.015585	0.311537 ± 0.010777	4.911065 ± 0.710956	1748 ± 53	1869 ± 248	94
2020.4	7	5	22	0.095798 ± 0.0096	0.297077 ± 0.010191	3.923975 ± 0.431247	1677 ± 51	1544 ± 189	109
2020.5	33	34	4	0.107098 ± 0.002804	0.302159 ± 0.008198	4.461895 ± 0.17842	1702 ± 41	1751 ± 48	97
2020.8	5	2	25	0.102212 ± 0.00969	0.307914 ± 0.010582	4.339441 ± 0.454761	1730 ± 52	1665 ± 176	104
SB32.1	12	6	12	0.102007 ± 0.004383	0.292347 ± 0.008577	4.111784 ± 0.226036	1653 ± 43	1661 ± 80	100
SB32.10	17	3	13	0.100677 ± 0.003805	0.294456 ± 0.008415	4.087457 ± 0.204991	1664 ± 42	1637 ± 70	102
SB32.12	2	4	44	0.100351 ± 0.041946	0.318639 ± 0.019142	4.408803 ± 1.894278	1783 ± 94	1631 ± 855	109
SB32.14	26	3	6	0.104011 ± 0.002045	0.312392 ± 0.008462	4.480035 ± 0.158604	1752 ± 42	1697 ± 36	103
SB32.15	14	3	11	0.10454 ± 0.003474	0.306102 ± 0.008767	4.412132 ± 0.205173	1721 ± 43	1706 ± 61	101
SB32.18	4	2	23	0.09542 ± 0.01161	0.302623 ± 0.01131	3.981481 ± 0.524265	1704 ± 56	1536 ± 231	111
SB32.20	17	4	9	0.101184 ± 0.003223	0.304495 ± 0.008672	4.248075 ± 0.192464	1714 ± 43	1646 ± 59	104
SB32.22	3	0	39	0.084433 ± 0.018003	0.289973 ± 0.012127	3.375774 ± 0.750634	1641 ± 61	1303 ± 424	126
SB32.24	16	5	9	0.100239 ± 0.003024	0.299714 ± 0.008436	4.142315 ± 0.181254	1690 ± 42	1629 ± 56	104
SB32.26	7	5	14	0.098915 ± 0.006588	0.304785 ± 0.00971	4.156769 ± 0.32147	1715 ± 48	1604 ± 124	107
SB32.4	12	4	12	0.107401 ± 0.004312	0.321089 ± 0.009485	4.754826 ± 0.250762	1795 ± 46	1756 ± 74	102
SB32.5.a	2	1	43	0.116382 ± 0.024399	0.312484 ± 0.014756	5.014351 ± 1.106077	1753 ± 72	1901 ± 385	92
SB32.8	6	5	20	0.089419 ± 0.008013	0.307853 ± 0.010124	3.795564 ± 0.37666	1730 ± 50	1413 ± 172	122

Supplementary data for manuscript No.1993e

Mineral chemistry

Mineral compositions of assemblages within metabasites and felsic shear zones were obtained using a Cameca SX51 Electron Microprobe, located at the University of Adelaide. Quantitative analyses were run at an accelerating voltage of 15 kV and a beam current of 20 nA.

1. Garnet

Mafic garnet analyses showed homogeneous compositions. Cores and rims typically have X_{Fe} (Fe/(Fe+Mg+Mn+Ca)) values ranging between 0.43 and 0.51. X_{Mg} values between 0.06 and 0.2. X_{Mn} values between 0.007 and 0.062 and X_{Ca} values between 0.31 and 0.41. Felsic garnet analyses also show homogeneous compositions with X_{Fe}'s of 0.66 to 0.8, X_{Mg} values between 0.03 and 0.13, X_{Mn} between 0.06 increasing to 0.27 in the cores and X_{Ca} values between 0.01 and 0.02.

2. Clinopyroxene

Clinopyroxene in all samples analysed plots within the diopside region of the Ca-Mg-Fe quadrilateral (Morimoto, 1989). X_{Mg} (Mg/(Mg+Fe) cations) is in the range 0.5 to 0.76. Among the non-quadrilateral components Al_2O_3 may be up to 5.1 wt.% but is typically below 4 wt.%. X_{jd} (Na/(Na+Ca+Mg+Fe_{tot}) component is never more than 0.09.

3. Hornblende

All amphibole is interpreted to be metamorphic in origin. All analysed amphiboles fall into the calcic amphibole group (Leake et al., 1997), having $Ca_B \geq 1.65$, $Na_B \leq 0.18$ and $(Ca+Na)_B \geq 1.65$. The majority of analysed amphiboles had $(Na+K)_A \geq 0.5$ and plotted within the ferropargasite-pargasite region on a X_{Mg} vrs Si diagram. The small subset which had $(Na+K)_A$ values <0.5 plotted within the ferrohornblende to magnesiohornblende field. Al_2O_3 content varies between 6.3 and 15.1 wt.%. SiO_2 between 38.8 and 49 wt.% and TiO_2 between 0.16 and 1.99 wt.%. X_{Mg} ranges from 0.26 to 0.67. The second generation of hornblende, which grew during post peak replacement of garnet, have low wt.% Ti and X_{Mg} values.

4. Mica

Biotite occurs in the felsic shear zones as a foliation defining mineral. X_{Na} (Na/Na+K) ranges between 0 and 0.15. X_{Fe} (Fe/Fe+Mg+Al^{VI}+Ti) is between 0.56 and 0.73, X_{Al}^{VI} between 0.08 and 0.2 and X_{Ti} between 0 and 0.04. Muscovite occurs as a retrograde mineral that overgrows the shear fabrics. X_{Na} (Na/Na+K+Ca) ranges from 0.02 to 0.03. X_{Fe} between 0.07 and 0.13, X_{Al}^{VI} between 0.84 and 0.92 and X_{Ti} of 0.

5 Feldspar

Metamorphic plagioclase from the mafic assemblages exhibits a complete solid solution from oligoclase to labradorite. An (Ca) content typically varies from An_{19} to

An_{67}. Plagioclase grains typically show core to rim zoning going to more An rich compositions (typically An_{25} in the core to An_{39} at the rim in sample SB3). From textural relationships it is likely that increasing anorthite content is related to the breakdown of the grossularite component of garnet.

Plagioclase from within the felsic shear zone fabrics tends to be predominantly albitic in composition with one sample being Al_{60} but the rest ranging between Al_{78} to Al_{98}. The K-feldspar component of the shear zones ranges in composition from Or_{87} to Or_{98} with a minor albite component constituting the remainder.

6. Ilmenite and Titanite

Ilmenite occurs in the mafic assemblages as both inclusions in titanite and within the first generation of metamorphic hornblende. Ilmenite contains an X_{Fe} (Fe/Fe+Mg+Mn) value between 0.85 and 0.98 with an Fe^{3+} component of approximately 0 up to 0.08 (Droop, 1987). X_{Mn} ranges between 0.01 up to 0.06 and an X_{Mg} of 0.

Titanite occurs as an abundant accessory mineral in the mafic assemblages and is interpreted to be metamorphic in origin. Titanite compositions are typically standard with only minor substitution of Al^{3+} and Fe^{3+} for Ti with X_{Al} (Al/Al+Fe+Ti) values between 0.03 and 0.05 and $X_{Fe\ values}$ between 0 and 0.02. Titanite also contains up to 34 ppm U and 36 ppm Th.